Myeloid cells contribute to bystander CD8 T cell accumulation in metabolic-associated steatohepatitis and are sufficient for fibrosis

Short title: Scar-associated macrophages fuel the immune-fibrosis niche

Authors

Cynthia Lebeaupin*[1], Katelyn L. Donahue*[1], Stephen M. Christensen[1], Shoh Asano[1], Marc H. Wadsworth II[1], Kathryn Bound[1], Saurav De[1], James McMahon[2], Franklin Schlerman[1], Chang Wang[1], Xiao Chen[1], Alexander M.S. Barron[1], Thomas A. Wynn[1], Kevin M. Hart[1], Thomas Fabre[1]

Affiliations

[1] Pfizer Inc., Cambridge, MA, USA.

**These authors contributed equally to this work as first authors.*

Corresponding author

Thomas.Fabre@pfizer.com

1 Portland Street, Cambridge MA, USA

Keywords

MASH, fibrosis, scar-associated macrophages, CXCR6/CXCL16

Graphical abstract

The immunopathological niche in fibrosis

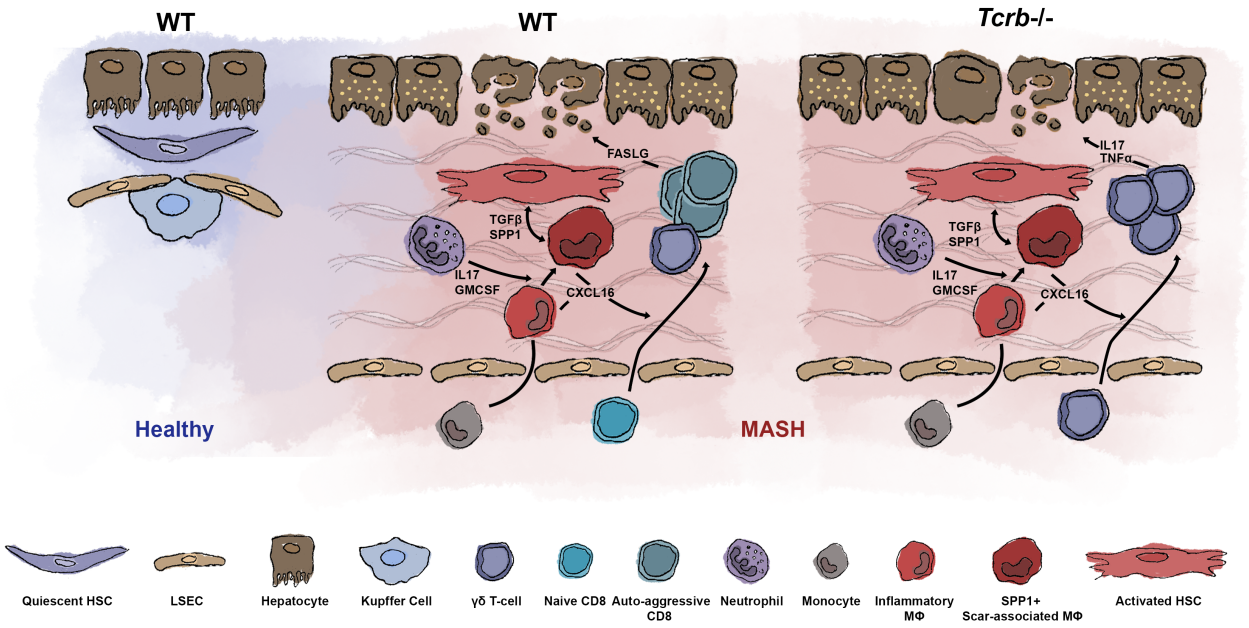

Highlights

- Adaptive and innate immune cells localize to the human MASH fibrotic niche
- CD8 T cells increase with MASH severity while MHC-II^{+} cells accumulate with fibrosis
- CXCR6^{+}FASLG^{+} CD8 auto-aggressive T cells accumulate at the scar
- CXCL16^{+} scar-associated macrophages retain CD8 T cells in the fibrotic MASH niche
- Liver injury, inflammation and fibrosis persist in the absence of conventional T cells
-

Impact and implications

Metabolic dysfunction-associated steatohepatitis (MASH) is a progressive liver disease in which fibrosis is a key determinant of patient outcomes and survival. This study demonstrates that fibrosis in MASH can develop independent of conventional T cell immunity, driven by myeloid cells including scar-associated macrophages (SAMs) and neutrophils within a localized hepatic niche in mice and humans. This highlights the need to prioritize innate immune mechanisms as key drivers of chronic (late-stage) liver disease for researchers and clinicians developing anti-fibrotic therapies.

Abstract

Background & Aims: Metabolic dysfunction-associated steatohepatitis (MASH) is a leading cause of liver fibrosis, morbidity, and mortality. It is characterized by the accumulation of fat in hepatocytes causing cell death followed by stromal cell activation and scar deposition at later disease stages. While a marked accumulation of cytotoxic CD8 T cells is observed in MASH in humans and mice, the role of adaptive immune cells in fibrosis progression remains debated.

Methods: Transcriptional data were curated from human datasets and preclinical mouse models, including mice deficient in TCRαβ T cells (*Tcrb*$^{-/-}$), which lack conventional CD4 helper and CD8 cytotoxic T cells, in diet-induced fibrosing MASH for single-cell RNA-sequencing. Specific human and mouse liver transcriptomic immune signatures were corroborated by flow cytometry and immunofluorescence.

Results: MASH was associated with the expansion of lymphocytes and myeloid cells. Auto-aggressive CXCR6^{+}PD1^{+}FASLG^{+} CD8 T cells were enriched in livers of high-fat-diet-fed mice and correlated with MASH and fibrosis. Notably, *Tcrb*-deficient mice in a chemical and dietary preclinical MASH model developed fibrosis to the same extent as wild-type mice and exhibited exacerbated pro-fibrotic type 3 inflammation. Loss of conventional CD8 T cells neither impacted myeloid cell number nor phenotype within the fibrotic niche. Neutrophil- and non-conventional lymphocyte-derived GM-CSF and IL-17A were central drivers in the fibrotic niche composed of pathogenic macrophages and activated myofibroblasts. Furthermore, myeloid cells were identified as the main source of CXCL16 in diseased livers, retaining auto-aggressive CD8 T cells to the scar and contributing to their accumulation. Thus, non-adaptive cells, including scar-associated macrophages (SAMs) and myofibroblasts, are sufficient for MASH-driven fibrosis in this model.

Conclusions: Targeting myeloid cells and fibroblasts should be prioritized as anti-fibrotic therapies for MASH.

65 **Introduction**

66

67 Fibrosis in metabolic dysfunction-associated steatohepatitis (MASH) represents a critical and
68 unresolved clinical challenge of chronic liver disease that will continue to rise over the next three
69 decades[1]. While recent advances in metabolic therapies show promise in reducing steatosis and
70 hepatocellular injury, fibrosis often persists[2,3]. MASH with fibrosis perpetuates due to a conserved,
71 self-perpetuating cycle of injury, inflammation, cell differentiation, and scarring[4]. A critical factor in
72 fibrotic progression and maintenance is the initiating inflammatory cascade. This involves the
73 recruitment and differentiation of innate immune cells (*e.g.,* monocytes to macrophages,
74 neutrophils) as well as the recruitment and activation of adaptive immune cells (*e.g.,* T cells),
75 leading to the establishment of a complex fibrotic niche[4].

76

77 Historically, the role of adaptive immunity in fibrosis has been contentious due to discrepancies
78 between preclinical models and human diseases. The involvement of adaptive immune cells (*e.g.,*
79 T and B cells) in viral hepatitis (HBV, HCV) and auto-immune hepatitis in humans is evident[5-10].
80 Auto- or viral-antigen-specific adaptive cells contribute to hepatocellular damage and activation
81 of myofibroblasts via both cytokine secretion and canonical cell death mechanisms (*e.g.,*
82 perforin/granzyme)[11-14]. In contrast, preclinical studies using carbon tetrachloride (CCl_4) or
83 dimethylnitrosamine (DMN)-induced liver injury in SCID and NOD/SCID mice demonstrated that
84 adaptive immunity was dispensable for fibrosis development[15,16]. However, the hepatotoxicity and
85 non-physiological mode of acute “sterile” chemical preclinical injury, such as CCl_4 and DMN, limits
86 the translational relevance and support of these findings. Moreover, the absence of adaptive
87 immunity in these settings may have altered the kinetics and quality of innate immune responses.
88 Despite these limitations, these foundational studies laid the groundwork for a broader
89 understanding of fibrosis as a maladaptive wound-healing response, potentially uncoupled from
90 classical adaptive immune pathways[17]. In the context of MASLD/MASH, perceived originally as a

91 “sterile” injury, more recent studies reported the expansion of Th2, Th17, Tregs and CD8 T cells
92 in liver biopsies, potentially resulting from dysbiosis and inflammation related to the peripheral
93 metabolic syndrome[11,18,19].
94
95 Investigations of adaptive immunity using diet-induced preclinical MASH models benefit from a
96 more organic, less “sterile” injury setting. In methionine and choline-deficient diet (MCDD)-
97 induced MASH, the ablation of $XCR1^+$ dendritic cells (DCs) decreased T cell activation and
98 reduced liver injury in mice[20]. In another report, choline-deficient high-fat diet (CDHFD) induced
99 the metabolic activation of CD8 T cells and NKT cells that promoted liver damage and MASH[19].
100 Recently, auto-aggressive $CXCR6^+PD1^+FASLG^+$ CD8 T cells that activate in response to calcium
101 influx rather than antigen recognition were shown to accumulate in high-fat diet- (HFD)-driven
102 MASH as well as human fibrotic livers. These auto-aggressive CD8 T cells exhibit transcriptional
103 profiles reminiscent of pathogenic T cells in chronic inflammatory diseases and mediate
104 FAS/FASLG-induced epithelial cell death[21]. However, these HFD models only showed modest
105 fibrosis induction and limited human validation. Furthermore, the contribution of auto-aggressive
106 T cells to fibrosis remains correlative, as the focus was on the composite non-alcoholic fatty liver
107 disease (NAFLD) activity score (NAS) and hepatoxicity, and the extent to which they are
108 necessary or sufficient for fibrogenesis remains unaddressed. Thus, while recent findings
109 implicate adaptive immunity in shaping hepatic inflammation, they fall short of establishing a
110 causal role in fibrosis progression.
111
112 Here, the role of conventional T cell-mediated adaptive immunity in the fibrotic niche was
113 interrogated by leveraging transcriptional and spatial profiling of human liver samples and
114 genetically modified mice lacking αβ T cells (*Tcrb-/-*) in a western diet-induced model of fibrosing
115 MASH. The findings of this study demonstrate that αβ T cells, while abundant in fibrotic tissue,
116 are not required for fibrosis progression. γδ T cells, with either an auto-aggressive-like or IL-17A

117 and TNFα phenotype, compensated in the absence of conventional T cells. Notably, the “core” of
118 the fibrotic niche appears to be independent of T cells and results from a myeloid-centric program
119 involving SPP1^{+} scar-associated macrophages (SAMs) and neutrophils that recruit CXCR6^{+} αβ
120 and γδ T cells and promote myofibroblast activation. These results challenge prevailing
121 assumptions about the immunological hierarchy in fibrosis and underscore the need to prioritize
122 innate immune mechanisms as therapeutic targets in chronic liver fibrotic disease.

Material and methods

Mouse strains and models

All procedures performed on animals were in accordance with regulations and established guidelines, which were reviewed and approved by an Institutional Animal Care and Use Committee and an ethical review process. All experimental procedures were performed at Pfizer (Cambridge, MA). C57BL/6J (WT) and *Tcrb*-/- (strain: 002118; The Jackson Laboratory, Bar Harbor, ME) male mice, starting at 6 weeks of age, were used for chemical (carbon tetrachloride; CCl_4) and/or diet-induced preclinical MASH (n= 6-15 per group). The mice were maintained in a thermo-neutral environment at a temperature of 30°C, humidity of 30-70%, and a 12 h-light/12 h-dark photocycle. Mice were injected with vehicle (olive oil) or CCl_4 (Sigma; 56-23-5 2x/week at 2 µl CCl_4/g) and/or fed a choline-deficient diet (CDA; Research Diets; A06071302) or HFD (Kcal of 40% fat, 20% fructose, and 2% cholesterol; D09100310; Research Diets, New Brunswick, NJ) for up to 40 weeks. Mice were euthanized using 5% CO2. Control animals were maintained on normal chow diet.

Human tissue sections

Human paraffin-embedded (FFPE) tissue sections were obtained anonymized from BioIVT with written informed consent. An institutional review board or independent ethics committee reviewed and approved relevant study documents, including the protocol. Study conduct adhered to the ethical guidelines of the 1975 Declaration of Helsinki principles, the Council for International Organizations of Medical Sciences international ethical guidelines, and all applicable laws and regulations. Human liver tissue samples sourced from vendors followed protocols that were reviewed and approved by appropriate regulatory and ethics committees. Patient metadata is available in Table S1.

149 **Tissue processing**

150 Livers from mice were collected on ice in cold RPMI 1640 medium, minced with a razor blade,
151 and collagenase-digested (100 U/ml; Sigma-Aldrich), shaking at 37°C for 1 h. After digestion, liver
152 tissues were filtered through 70 μm nylon mesh. Hepatocytes were removed by slow
153 centrifugation (50 g for 5 min) and non-parenchymal cells were enriched by centrifugation through
154 a 25% Percoll (GE Life Sciences) gradient at 850 g for 15 min. Erythrocytes were lysed with
155 ammonium-chloride-potassium buffer (Thermo Fisher Scientific). Cells were subsequently
156 distributed either for flow cytometry, restimulation with PMA/Ionomycin, or scRNA-seq.

157

158 **Multiplex cytokine analysis**

159 Intrahepatic leukocytes (IHLs) were resuspended at a concentration of 5 million cells per ml in
160 RPMI with 10% fetal bovine serum (FBS) and 1× stimulation cocktail (eBioscience) for 18 h.
161 Supernatants were collected and stored at -80°C. Multiplex cytokine/chemokine quantification
162 was performed using 25 μl of supernatant post-stimulation (LEGENDplex; BioLegend). Analysis
163 was performed using BioLegend Cloud analysis software. Data were expressed as fold change
164 normalized to control, chow-fed mice.

165

166 **Flow cytometry**

167 Mouse and human cells were washed with phosphate-buffered saline (PBS) and stained for 20
168 min at room temperature with LIVE/DEAD fixable aqua viability dye (Invitrogen). Cells were
169 washed with fluorescence-activated cell sorting (FACS) buffer and subsequently fixed with
170 Foxp3/Transcription Factor Fixation/Permeabilization buffer (Invitrogen). After washing
171 (PermWash Buffer; Invitrogen), cells were resuspended in freezing solution (90% FACS
172 buffer/10% dimethyl sulfoxide (DMSO)) and stored at -80°C. Once thawed, cells were washed,
173 and Fc receptors were blocked with TruStain FcX (mouse or human, as appropriate; BioLegend)
174 before staining with antibodies from Table S2. Cells were then washed, filtered through 60 μm

175 mesh, and run on a BD FACSymphony flow cytometer (BD). Data were analyzed with Omiq.ai,
176 using a DownSample and UMAP (Uniform Manifold Approximation and Projection) workflow.
177
178 **cycIF staining and analysis**
179 Human and mouse cyclic immunofluorescence (cycIF) was performed as described[22,23], using
180 antibodies listed in Tables S3 or S4, respectively . Briefly, human or mouse liver FFPE sections
181 were deparaffinized, rehydrated, and subjected to heat-induced (Citrate PH 6) epitope antigen
182 retrieval. Slides were stained at 4°C overnight with primary antibodies in blocking buffer solution
183 (PBS, 0.05 % Tween-20, 5% bovine serum albumin, 0.1% Triton X-100). After three washes (PBS,
184 0.05% Tween-20), slides were stained with fluorescently conjugated donkey secondary antibodies
185 (diluted 1:500 in blocking buffer) for 1 h at RT. Slides were again washed, DNA-stained with 4′,6-
186 diamidino-2-phenylindole (DAPI; Invitrogen), and mounted in EverBrite Trueblack mounting
187 medium to reduce auto-fluorescence. Acquisition was performed on an Axioscan Slide Scanner
188 (Zeiss). Following imaging, coverslips were removed and antibodies were stripped for subsequent
189 rounds of staining. For image processing, acquired images were first subjected to shading
190 correction and stitching using the Zeiss ZEN blue DESK (version 3.0) image processing software.
191 Alignment across subsequent rounds was performed on their respective nuclear (DAPI) channel
192 in QuPath by applying the transformation to the remaining channels[24,25]. The multichannel image
193 pyramid was generated using Bioformats2Raw and Raw2OMETiff programs (Glencoe Software,
194 Seattle, WA) and before conversion into FCS for analyses in Omiq.ai.
195
196 **Fibrosis histology**
197 FFPE sections were deparaffinized and incubated for 30 min in Picro Sirius Red fast green
198 solution (Direct Red 81 0.2%, FCF 0.1% in 1.3% picric acid solution, Sigma-Aldrich). Sections
199 were vigorously rinsed in dH_2O, dried, mounted with Permount (Thermo Fisher Scientific), and
200 acquired on an Axioscan Slide Scanner (Zeiss) in brightfield and with polarized light.

201

202 **TUNEL staining**

203 Cell death was assessed using the ApopTag Peroxidase *In Situ* Apoptosis Detection Kit (Millipore-
204 Sigma, S7101), following the manufacturer's instructions. Briefly, mouse liver FFPE sections were
205 deparaffinized, pretreated with proteinase K and quenched with endogenous peroxidase followed
206 by the addition of equilibration buffer directly on each specimen. Slides were incubated with TdT
207 enzyme in a humidified chamber at 37°C for 1 h, washed, and an anti-digoxignenin conjugate was
208 applied to the slides kept in a humidified chamber for 30 min at room temperature. After additional
209 PBS washes, peroxidase substrate developed the color, slides were washed, and a methyl-green
210 counterstain was applied. Specimens were dehydrated with xylene and slides mounted with
211 Permount. Brightfield slide images were acquired on an Axioscan Slide Scanner (Zeiss) and
212 TUNEL-positive staining was quantified in QuPath.

213

214 **Immuno-histochemistry**

215 FFPE slides were deparaffinized, rehydrated, and subjected to antigen retrieval as described
216 above for cycIF. Endogenous peroxidases were quenched for 15 min at RT with 0.6% H_2O_2 in
217 MeOH. Slides were washed three times (dH_2O x2 followed by PBS x1), then incubated overnight
218 in a humidified chamber in blocking buffer solution with anti-CD3e (Abcam, Rabbit host, cat#
219 ab16669 and Invitrogen, Rat host, cat# MA5-16622, both 1:50) at 4°C. The following day, slides
220 were washed with PBS three times and then incubated for 45 min at RT with biotinylated
221 secondary antibodies (Goat anti-Rabbit IgG, Invitrogen, cat#65-6140 and Goat anti-Rat IgG,
222 Vector Laboratories, cat#BA-9401-.5) diluted 1:300 in blocking buffer. The Vectastain Elite ABC
223 Kit, Peroxidase (Vector Laboratories, cat#PK-6100) was applied following the manufacturer's
224 protocol for 30 min at RT. Slides were developed for ~20 min using the DAB Substrate Kit
225 Peroxidase (Vector Laboratories, cat#SK-4100). Slides were washed in dH_2O and counterstained
226 with Modified Mayer's Hematoxylin (Epredia, cat#72804) for 2 min at RT. Slides were rinsed in

227 dH_2O and PBS sequentially and then dehydrated in 95% EtOH for 10 sec x2, 100% EtOH for 2
228 min x2, and xylene for 2 min x2 before mounting with Permount and drying overnight prior to
229 brightfield imaging on an Axioscan Slide Scanner (Zeiss).
230

231 **Mouse scRNA-seq and data analyses**

232 Cells from murine tissues were dissociated as described above, fixed in methanol following the
233 10X Genomics fixation protocol, and stored at -80°C (10X Genomics, Pleasanton, CA). A 3'
234 sequencing library was generated following protocols from 10x Genomics Single cell version 3.1.
235 Samples from WT animals were sequenced on an Illumina NextSeq 2000. Samples from the *Tcrb*-
236 /- animals were lipid-hashed as described[26] and sequenced on an Illumina NextSeq 500. FASTQs
237 were preprocessed and aligned with Cell Ranger version 8.0.1 using the mouse reference
238 GRCm39-2024-A. Downstream processing of count matrices was performed using Seurat version
239 5.1.0[27] and R version 4.4.0. Ambient RNA was corrected using SoupX version 1.6.2[28]. Samples
240 with lipid hashing were demultiplexed according to the Seurat workflow using HTODemux[29] with
241 positive.quantile = 0.95. Wild-type (WT) and *Tcrb*-/- samples were merged and subjected to QC
242 assessment using the Add_Cell_QC_Metrics functionality from scCustomize version 3.0.1
243 (RRID:SCR_024675, https://zenodo.org/records/17575311). Following uniform filtration, samples
244 were split into WT and *Tcrb*-/- groups and analyzed in parallel following the Seurat workflow with
245 the following modifiactions. Data were normalized with SCTransform with vars.to.regress =
246 "nCount_RNA"[30]. PC utilization was determined by assessing both the number of dimensions that
247 capture ~90% variance and the point at which change in variation between PCs became <0.1%.
248 Cells of interest (lymphocytes and myeloid cells) were subset from global objects, renormalized
249 and clustered as described above, and filtered for contaminating cell types. Gene signature
250 visualization was done with Nebulosa version 1.14[31].
251
252

253 **Deconvolution with BayesPrism and immune cell signature analysis**

254 Pre-processed scRNA-seq data of all cells from study GSE192742 were obtained from the
255 cellxgene initiative (https://cellxgene.cziscience.com/collections/74e10dc4-cbb2-4605-a189-
256 8a1cd8e44d8c) and pre-processed raw RNA-seq counts were obtained from GEO for study
257 GSE135251. *CD8A* and *CD4* expression was used to identify CD8 T and CD4 T cells in the T cell
258 cluster respectively using Seurat package[32]. To understand the cellular composition in samples
259 from healthy donors and patients with NAFLD and NASH, we applied BayesPrism[33] to predict the
260 abundance of cell types by modeling gene expression levels through bulk RNA-Seq data. Input
261 into BayesPrism included the raw counts from the bulk tissue and scRNA-seq normalized counts
262 from GSE192742 as a reference. Predicted cell type specific expression from BayesPrism was
263 normalized using variance stabilizing transformation using DESeq2 package[34]. Immune and
264 Kupffer cell gene sets were scored in the raw counts from the bulk tissue using the z-score method
265 in the hacksig package[35]. We applied linear regression to evaluate the association between
266 abundances of cell types, counts per million (CPM) of select genes and cell signature scores with
267 endpoints including age, histopathological stage and grade adjusting for batch and center as
268 covariates.

269

270 **Hydroxyproline quantification**

271 Liver and lung hydroxyproline content was quantified as previously described[11]. Tissues (100 to
272 200 mg) were hydrolyzed in 1 ml of 6 N HCl at 110°C overnight. Ten microliters of the hydrolyzed
273 sample or standard were placed in 30 µl of citric acetate buffer [10 g of citric acid (5%, w/v), 2.4
274 ml of glacial acetic acid (1.2%, v/v), 14.48 g of sodium acetate (7.24%, w/v), and 6.8 g of sodium
275 hydroxide (3.4%, w/v) with a total volume of 200 ml made up with sterile deionized water]. One
276 hundred microliters of chloramine T solution (0.282 g of chloramine T, 2 ml of isopropanol, 2 ml of
277 sterile water, and 16 ml of citrate acetate buffer) were mixed with the samples or standards and
278 oxidized for 20 min at room temperature. Oxidized samples or standards received 100 µl of

279 Ehrlich's reagent (2.5 g of *p*-dimethylaminobenzaldehyde, 9.3 ml of isopropanol, and 3.9 ml of
280 70% perchloric acid) and incubated at 65°C for 20 min. Optical density at 550 nm was recorded
281 and compared with the standard curve for quantification.
282
283 **Statistical analysis**
284 Statistical tests were conducted using R v4.4.0 (https://r-project.org/) or GraphPad Prism v10
285 (GraphPad Software, La Jolla, CA). Testing for differential expression was performed in R using
286 Seurat v5.1.0 and CellChat version 2.1.2. Graphs were generated in GraphPad Prism, the R
287 packages Seurat v5.1.0[36], ggplot2 version 3.5.1, scCustomize version 3.0.1, and Nebulosa
288 version 1.14.0[31] in R version 4.4.0, QuPath, or Omiq.ai. Differences were determined between
289 two groups by Mann-Whitney test or between greater than two groups by analysis of variance
290 (ANOVA) followed by Tukey post-hoc test.

291 **Results**

292 **Adaptive and innate immune cells are enriched in the fibrotic niche of human MASH**

293 To investigate immune cell proportions in human fibrotic MASH livers, a bulk RNA-seq dataset
294 consisting of over 200 NAFLD, now referred to as metabolic dysfunction-associated steatotic liver
295 disease (MASLD), patient biopsies[37] (GSE135251) was deconvoluted to predict liver non-
296 parenchymal cell (NPC) fraction frequencies from patients stratified by fibrosis stage (F0-F2 vs
297 F3-F4) (Figure 1A). This analysis revealed a significant increase in the predicted frequency of
298 CD8 T cells in patients with high Non-Alcoholic Steatohepatitis Activity Score (NAS; 6-8) or severe
299 fibrosis (F3-F4) (Figure 1B). Immunofluorescence (IF) of human liver sections delineated α-SMA$^+$
300 scar regions, which were enriched for CD3$^+$, CD8$^+$, and MHC-II$^+$ cells in patients with severe (F3-
301 F4) compared to minimal (F1-F2) fibrosis (Figure 1C). Cyclic immunofluorescence (cycIF) was
302 performed to quantify frequencies of CD3$^+$CD8$^+$ T cells and MHC-II$^+$ myeloid cells within liver scar
303 regions (Figure 1D-F). Increased CD3$^+$CD8$^+$ T cell percentages were significantly associated with
304 higher NAS (driven by lobular inflammation and ballooning) and fibrosis (Figure 1E,F),
305 corroborating the bulk deconvolution results (Figure 1B). Conversely, MHC-II$^+$ cell enrichment was
306 specific to fibrosis severity and did not vary with other NAS parameters (Figure 1E,F). Collectively,
307 these data establish that both adaptive and innate immune cells are spatially localized to the
308 fibrotic niche in human MASH livers, though they associate with distinct disease hallmarks.

309

310 **Auto-aggressive CD8 T cells accumulate in human fibrotic MASH and are associated with**
311 **disease severity**

312 Bulk RNA-seq datasets (GSE135251) were used to build on the established model of auto-
313 aggressive CXCR6$^+$ CD8 T cell-mediated, FASLG-dependent hepatocyte death in MASH[21]. *FAS*
314 gene expression was significantly increased in patients with high NAS or advanced fibrosis
315 (Figure 2A), while *FASLG*, which is expressed by NK cells and ILC1s in addition to T cells, neither
316 correlated with NAS nor fibrosis (Figure 2B). Deconvoluted CD8 T cells, as characterized in Figure

317 1A, were then scored with an auto-aggressive CD8 T cell signature, as previously described[21].
318 CD8 T cells from patients with high NAS or advanced fibrosis were enriched for the auto-
319 aggressive CD8 T cell signature (Figure 2C). Robust FASLG protein expression was confirmed
320 by IF in fibrotic regions, co-localizing with $CD3^+$ and $CD8^+$ immune cells (Figure 2D,E). FASLG
321 intensity was highest within CD8 T cells (Figure 2E), with the abundance of $FASLG^+$ CD8 T cells
322 increased in livers from patients with high NAS (driven by lobular inflammation) or those with
323 advanced fibrosis (Figure 2F,G). These data suggest that auto-aggressive, FASLG-expressing
324 CD8 T cells accumulate in the fibrotic niche in human MASH and may contribute to progressive
325 liver injury.
326
327 **CD8 T cells preferentially accumulate in preclinical models of fibrosing MASH**
328 The presence of T cells was further characterized across preclinical MASH and fibrosis models
329 induced in *C57BL/6* wild-type (WT) mice at 6 weeks of age by chemical compounds (*i.e.,* CCl_4)
330 and/or dietary regimens (*i.e.,* choline-deficient (CDA) or HFD consisting of 40% fat, 20% fructose,
331 2% cholesterol). Fibrosis was present in all mice, as assessed by picro Sirius Red staining and
332 imaged by either brightfield or polarized light, the latter providing improved and specific
333 visualization of intercellular fibrosis (Figure 3A). Lymphocytes, identified by CD3 IHC staining,
334 accumulated around the “crown like” structures of fatty hepatocytes (Figure 3B), consistent with
335 the reported auto-aggressive T cell function of killing lipid-laden hepatocytes in proximity[21]. The
336 proportion of CD8 T cells was significantly increased only in MASH livers with significant steatosis,
337 such as CDA and HFD, but not CCl_4 alone (Figure 3C). Thus, the 40-week HFD model, mimicking
338 MASH with fibrosis and enrichment of CD8 T cells, was selected as the optimal model for this
339 study[38]. Single-cell RNA-seq (scRNA-seq) profiling of chow and HFD livers at 40 weeks revealed
340 a diverse immune landscape (Figure 3D, Supplementary Figure 1A,B). Livers of HFD-fed mice
341 exhibited marked increases in the frequencies of CD8 T cells and myeloid cells (*i.e.,*

342 monocytes/macrophages, dendritic cells), reflecting an exacerbated inflammatory state (Figure
343 3E), similar to human disease.
344
345 **CD8 T cells display distinct transcriptional and phenotypic features linked with auto-**
346 **aggression and activation in livers of chronic HFD-fed mice**
347 To further characterize adaptive inflammation in HFD-fed mice, lymphocytes from scRNA-seq
348 were subclustered and annotated (Figure 4A, Supplementary Figure 2A). Remodeling of the
349 lymphocyte landscape in livers of HFD-fed mice was evident by the increase of mature CD8 T cell
350 subsets and reduction of naive and tissue-resident populations compared to chow-fed mice
351 (Figure 4B). Auto-aggressive CD8 T cells were delineated using joint density approximation
352 defined by a signature of key functional markers previously described (*Cxcr6*, *Il2rb*, *Pdcd1*, *Fasl*,
353 *Cd3e*)[21] (Figure 4C). To complement these transcriptomic observations, protein expression on
354 CD8 T cells was profiled by UMAP dimensionality reduction and unbiased clustering of flow
355 cytometry data (Figure 4D, E). Ten phenotypically distinct CD8 T clusters were identified (C1-C10)
356 (Figure 4D), with clusters C1, C6-C10 predominantly enriched in livers of HFD-fed mice (Figure
357 4D, E). Cluster C1 presented high expression of auto-aggressive and exhaustive CD8 T cell
358 markers, including FASLG and PD1, respectively (Figure 4F). Chronic HFD increased the
359 frequency of $CD44^{+}FASLG^{+}CXCR6^{hi}$ CD8 T cells, reduced homeostatic tissue-resident
360 macrophage- (TRM)-like cells ($CD69^{+}PD1^{+}$), and drove effector populations toward an exhausted
361 phenotype ($CD69^{-}PD1^{+}$) (Figure 4G-J).
362
363 **Livers of HFD-fed *Tcrb*-deficient mice show persistent cell death and scarring with rebound**
364 **γδ T cell accumulation**
365 To assess the therapeutic potential of autoimmunity disruption in chronic diet-induced liver injury
366 and fibrosis, *Tcrb*-deficient mice (*Tcrb*-/-), which lack conventional TCRαβ T cells, were challenged
367 with the 40-week HFD. All HFD-fed mice exhibited progressive weight gain, with *Tcrb*-deficient

368 mice showing a modest but significant reduction in body weight increase compared to WT
369 counterparts (Figure 5A,B). Liver index was comparable between genotypes and remained
370 markedly elevated relative to chow-fed baseline (dotted line, Figure 5C). Serum transaminases
371 (*i.e.,* ALT and AST) were lower in HFD-fed *Tcrb*-deficient compared to WT mice (~450 and ~600
372 ALT U/L, respectively), but remained higher than chow-fed baseline levels (~50 ALT U/L),
373 indicating persistent hepatocellular injury (Figure 5D,E). Histological assessment revealed
374 extensive steatosis and collagen deposition in both WT and *Tcrb*-deficient mice fed HFD, with no
375 significant difference in fibrosis (Figure 5F,I). Although liver injury was reduced, cell death
376 assessed by TUNEL^{+} staining was increased in *Tcrb*-deficient mice (Figure 5G,J), while cleaved
377 Caspase-3 showed no significant change (Figure 5H,K), contrasting with previous reports in mice
378 lacking both conventional αβ and γδ T cells (*Tcrb/d*-/-)[21]. As expected, *Tcrb*-deficient mice lacked
379 conventional CD8 T cells; however, this was accompanied by a significant rebound or
380 compensatory accumulation of intrahepatic γδ T cells (Figure 5L). These data demonstrate that
381 the loss of TCRαβ cells did not mitigate chronic HFD-induced cell death or fibrosis, but rather
382 promoted alternative and potentially compensatory T cell responses.
383
384 **HFD-fed *Tcrb*-deficient mice present exacerbated hepatic pro-fibrotic type 3 inflammation**
385 Liver samples from *Tcrb*-deficient mice fed control chow or HFD were also profiled by scRNA-seq
386 (Supplementary Figure 3A-D) and intrahepatic lymphocytes were subclustered, revealing a
387 diverse γδ T cell compartment (Figure 6A, Supplementary Figure 3E). Notably, application of the
388 functional auto-aggressive signature (*Cxcr6*, *Il2rb*, *Pdcd1*, *Fasl*, *Cd3e*) identified a population of
389 γδ T cells with transcriptional similarity (Figure 6B). Furthermore, a cluster with co-localized
390 expression of type 3 cytokines, namely *Il17a* and *Tnf,* was highly prevalent during chronic HFD
391 (Figure 6A-C). Intrahepatic leukocytes (IHLs) were then isolated and restimulated from WT and
392 *Tcrb*-deficient livers for functional assessment of cytokine output (Figure 6D). Compared to WT,
393 HFD-fed *Tcrb*-deficient mice released increased levels of type 1 pro-inflammatory (IL6, TNFα) and

394 type 3 pro-fibrotic (IL17A, GMCSF) factors, alongside T cell-inducing cytokines (IL-12p40, IL-
395 12p70, IL-23a), but not type 2 cytokines (IL-5) (Figure 6D,E). Particularly, IL6, IL-17A and TNFα
396 were significantly elevated in IHLs from HFD-fed *Tcrb*-deficient mice (~550, ~1000 and ~600
397 pg/mL, respectively) when compared to their WT counterparts (~175, ~600 and ~100 pg/mL,
398 respectively) (Figure 6E). These findings suggest that the absence of conventional CD8 T cells
399 promotes compensatory γδ T cell expansion in the liver and a pro-fibrotic cytokine milieu
400 dominated by IL-17A and TNFα, which may synergize to drive hepatotoxicity and fibrotic
401 remodeling.
402
403 **Pro-fibrotic SPP1$^+$ scar-associated macrophages (SAMs) persist in MASH livers in the**
404 **absence of conventional αβ T cells**
405 Given that *Tcrb*-deficiency failed to prevent HFD-induced fibrosis in mice, myeloid subsets were
406 subsequently investigated. Livers of HFD-fed mice analyzed by scRNA-seq revealed an increase
407 in myeloid diversity in HFD-fed animals compared to chow-fed controls of both WT and *Tcrb*-
408 deficient mice (Figure 7A-F, Supplementary Figure 4A,B). In both genotypes, HFD increased the
409 abundance of SPP1$^+$ SAMs, defined by the expression of the Fab5 signature (*Cd9*, *Trem2*, *Cd63*,
410 *Fabp5*, *Gpnmb*, *Spp1*)[23] (Figure 7B,E). The presence of SPP1$^+$ SAMs was assessed at the protein
411 level by flow cytometry, where HFD led to the specific accumulation of CD9$^+$TREM2$^+$Galectin-
412 3$^+$GPNMB$^+$ cells within F4/80$^+$Ly6C^{lo} macrophages, in both WT and *Tcrb*-deficient mice (Figure
413 7G). While the relative abundance of myeloid cells was consistent across conditions, HFD led to
414 a significant increase in CD9$^+$TREM2$^+$Galectin-3$^+$GPNMB$^+$ macrophages compared to normal
415 chow, irrespective of genotype (Figure 7H). Heatmap profiling of flow cytometry-based protein
416 expression further showed the upregulation of SAM-specific markers in fibrotic livers of HFD-fed
417 mice, with comparable expression patterns between WT and *Tcrb*-deficient mice (Figure 7I).
418 Finally, cycIF of WT and *Tcrb*-deficient HFD livers showed a fibrotic niche architecture
419 characterized by the accumulation of GMCSF$^+$IL17A$^+$MMP9$^+$ neutrophils, SPP1$^+$GPNMB$^+$FABP5$^+$

420 SAMs[23], and RBPJ$^+$ macrophages[39] in proximity of Desmin$^+$ myofibroblasts forming crown-like
421 structures (Figure 7J). Thus, HFD-induced SPP1$^+$ SAM expansion in liver disease occurs
422 independently of conventional αβ T cells, implicating macrophage-driven mechanisms in fibrosis
423 persistence.
424
425 **CXCL16 positive myeloid cells retain CD8 T cells in fibrotic niches of human and mouse**
426 **liver**
427 Transcriptomic cell-cell interaction analysis predicted a significant increase in the number of
428 ligand-receptor communications between T cells and myeloid cells in livers of both WT and *Tcrb*-
429 deficient HFD-fed mice compared to chow-fed controls (Figure 8A). Interactions were filtered to
430 chemokine/receptor pairs upregulated in HFD and revealed CXCL16 and CXCR6 as a preserved
431 chemotactic axis between myeloid cells and both αβ and γδ T cells within fibrotic liver tissue
432 (Figure 8B). These findings were confirmed using human liver tissue from MASH patients with
433 either early-stage disease (F0-F2) or advanced fibrosis (F3-F4). Increased CXCL16$^+$ and
434 GPNMB$^+$ macrophages were observed by IF in α-SMA$^+$ fibrotic regions (Figure 8C). CycIF
435 analysis confirmed CXCL16$^+$ localization in scar regions co-populated by CD8 T cells and SPP1$^+$
436 SAMs (Figure 8D). Spearman correlation between the frequencies of cells identified by cycIF and
437 components of NAS and fibrosis revealed a positive correlation between CXCL16$^+$ cells and the
438 accumulation of both total and FASLG$^+$ CD8 T cells in human MASH livers (Figure 8E,F).
439 Moreover, the frequency of SPP1$^+$GPNMB$^+$FABP5$^+$ SAMs correlated specifically with fibrosis,
440 over other histological features (NAS and steatosis), supporting their pro-fibrotic nature (Figure
441 8G,H). These findings identify CXCL16-CXCR6 signaling as a key mechanism by which SAMs
442 and other myeloid cells orchestrate immune cell positioning, recruiting T cells within the fibrotic
443 microenvironment. Myeloid cells, particularly through SAM expansion, contribute to bystander
444 CD8 and γδ T cell accumulation in MASH and are thus sufficient for liver fibrosis.

445 **Discussion**

446 The immunopathological landscape of MASH has often featured the accumulation of T cells, due
447 to the metabolic syndrome, dysbiosis and hepatocellular cell death triggering chemotactic
448 responses to the liver[4]. T cells contribute to fibrosis progression via either pro-inflammatory and
449 pro-fibrotic cytokine secretion or cytotoxic pathways. We and others reported the dysregulation of
450 the T effector (Th2/Th17) to T regulatory cell ratio in MASH, contributing to the pro-fibrotic type 2
451 and 3 mixed inflammatory milieu[11,18]. MASH livers also feature a lipotoxic environment that affects
452 survival of CD4 T cells and leads to a significant accumulation of CD8 T cells[19]. Here, we
453 confirmed first by deconvolution of a bulk RNA-seq dataset of over 200 patients (Figure 1A,B)
454 and in an independent cohort of FFPE MASH livers using cycIF (Figure 1C-E) that CD8 T cell
455 accumulation in the liver correlates with NAS, lobular inflammation and fibrosis stage. CD8 T cells
456 may expand in livers due to the presence of $XCR1^+$ cDC1s, and chronic antigenic stimulation,
457 promoting inflammation and hepatocellular damage[20,40]. Liver homing/resident $CXCR6^+$ CD8 T
458 cells, rendered auto-aggressive through IL-15-driven transcriptional reprogramming and
459 metabolic activation, were reported to contribute to FASLG-mediated hepatocyte apoptosis in
460 preclinical models of MASH[21]. This auto-aggressive signature was significantly enriched in livers
461 with high NAS (6-8) and fibrosis (F3-4), as demonstrated by deconvoluted bulk RNA-seq (Figure
462 2C). Using cycIF, we confirmed that auto-aggressive CD8 T cells (defined by the co-expression
463 of FASLG, CD3 and CD8) correlated with lobular inflammation and were enriched in fibrotic scars
464 (Figure 2D-G) in human MASH livers.

465

466 In line with previous reports, CD3 T cells were located in areas of fibrosis in both toxin- and diet-
467 induced fibrosis models (Figure 3A, B). However, the frequency of CD8 T cells was significantly
468 increased only in models with severe and chronic steatohepatitis such as CDA and HFD. This
469 could explain the previous observation that adaptive immune cells may not contribute to fibrosis
470 in toxin-dependent preclinical models. Indeed, expansion of CD8 T cells in MASH appears to be

471 clonal[40], as a result of lipid accumulation in the liver and potential dysbiosis. Additionally, scRNA-
472 seq and flow cytometry confirmed that chronic western-diet (high fat, fructose and cholesterol)
473 induced an auto-aggressive CD8 T cell phenotype ($CD44^{hi}CXCR6^{+}FASLG^{+}PD1^{+}$), as previously
474 reported using CDHFD[21]. Genetic ablation of conventional αβ T cells using *Tcrb*-deficient mice
475 led to a modest improvement of certain physiopathological features of MASH, such as percent
476 body weight and serum ALT (Figure 5A-D). However, serum ALT remained nearly ten times higher
477 than mice on chow diet, which was consistent with the lack of improvement in cell death, assessed
478 by $TUNEL^{+}$ and cleaved-Caspase-3^{+} cell counts, in livers of HFD-fed *Tcrb*-deficient mice (Figure
479 5G,H,J,K). Foreseeably, this was associated with no significant improvement in fibrosis, as
480 determined by both picro Sirius Red staining and hydroxyproline quantification (Figure 5F,I).
481 These results contrast with the recent observation linking both CD4 and CD8 T cells to the
482 amplification of inflammation and fibrosis in MASH[41].
483
484 The contribution of γδ T cells in the liver has been linked to both fibrosis progression and
485 resolution, depending on their phenotype. These γδ T cells can limit hepatocellular death via the
486 secretion of IL-22, activation of hepatic stellate cells (HSCs) via the secretion of IFNγ, and mediate
487 clearance of activated HSCs via FAS/FASLG[42]. The role of auto-aggressive CD8 T cells in MASH
488 was initially defined in mice lacking both αβ and γδ T cells (*Tcrb/d*-double-deficient)[21]. In our case,
489 a significant compensatory rebound in γδ T cells in livers of *Tcrb*-deficient mice was observed
490 after chronic HFD (Figure 5L). The γδ T cells in HFD-fed *Tcrb-/-* mice displayed a diverse array of
491 pro-fibrotic phenotypes, including a cell cluster enriched for the functional auto-aggressive
492 signature (*Cxcr6*, *Il2rb*, *Pdcd1*, *Fasl*, *Cd3e*), originally described in CD8 T cells. Another cluster of
493 γδ T cells showed co-expression of *Il17a* and *Tnf,* consistent with the significantly higher level of
494 IL-17A, GMCSF and TNFα in re-stimulated IHLs from *Tcrb*-deficient mice when compared to WT
495 mice following 40 weeks of chronic HFD (Figure 6D,E). Notably, IL-17A is a pro-inflammatory and
496 pro-fibrotic cytokine associated to fibrosis progression in many types of liver injury and tissues.

497 IL-17A facilitates TNF-driven hepatotoxicity in steatotic hepatocytes, amplifying Caspase-2-
498 SREBP1/2-mediated lipogenesis and inflammation[43,44]. IL-17A also sensitizes HSCs to the action
499 of TGFβ via stabilization of the TGF-β-RII on the surface. Altogether, our results indicate that γδ
500 T cells expand in the absence of conventional αβ T cells and maintain a milieu favorable, skewed
501 towards type 3 inflammation, to the development of the fibrotic niche[45].
502
503 Fibrotic scars of both WT and *Tcrb*-deficient mice showed myeloid cell dysregulation, particularly
504 characterized by the loss of tissue-resident Kupffer cells and accumulation of SPP1$^+$ SAMs with
505 a Fab5 signature[23]. Lack of conventional αβ T cells neither impacted the overall frequency,
506 transcriptomic signature nor phenotype of SPP1$^+$ SAMs (Figure 7A-I). Histologically, scars from
507 WT and *Tcrb*-deficient mice showed similar accumulation of IL17A$^+$GMCSF$^+$MMP9$^+$ neutrophils
508 in proximity of myofibroblasts and SPP1$^+$GPNMB$^+$FABP5$^+$ macrophages. SPP1$^+$ SAMs are
509 associated with fibrosis progression across tissues, degrade normal extracellular matrix (ECM;
510 Collagen IV) and increase deposition of pathogenic ECM (Collagen I)[23]. Accordingly, these cells
511 accumulated in human MASH livers with severe fibrosis at the scar border and correlated with
512 histopathological fibrosis grade (Figure 8C,D,H). Unlike CD8 T cells, SPP1$^+$ SAMs neither
513 correlated with increased NAS, lobular inflammation, hepatocyte ballooning nor steatosis (Figure
514 8G), reinforcing their pro-fibrotic association. Moreover, we found increased protein expression of
515 RBPJ (Figure 7J), a transcription factor involved in pathogenic monocyte to macrophage (MDM)
516 differentiation, in myeloid cells associated with fibrosis in livers from HFD-fed mice[39].
517
518 Finally, we investigated whether myeloid cells in the liver fibrotic niche may contribute to the
519 accumulation of CXCR6$^+$ T cells during MASH. Unbiased chemokine/receptor interaction
520 predictions identified a conserved mechanism of myeloid-driven T cell recruitment to the fibrotic
521 niche in livers of both *Tcrb*-deficient and WT HFD-fed mice (Figure 8A,B). These data show that
522 macrophages/monocytes and dendritic cells are sources of CXCL16 that bind CXCR6 on auto-

523 aggressive CD8 T cells and γδ T cells. Taken together, these results indicate that myeloid cells,
524 rather than conventional adaptive immune cells, are pivotal regulators of inflammation at the
525 fibrotic niche. While broad neutralization of myeloid cells via inhibition of CCR2 showed limited
526 efficacy in patients, due to its broad effect, it is possible that more refined myeloid cell inhibition
527 would be beneficial[46-50]. Preventing monocyte recruitment by CCR2 antagonism not only limits
528 the development of pathogenic MDMs, but also the ability of monocytes to restore the pool of
529 depleted tissue resident macrophages (*i.e.,* Kupffer cells) in MASH. As an alternative therapeutic
530 approach, myeloid cell inhibition of RBPJ blunted differentiation towards $SPP1^+$ SAMs, improved
531 recovery of Kupffer cells and induced patrolling monocytes, reducing inflammation and fibrosis in
532 preclinical MASH models[39].
533
534 This study contextualizes the roles of adaptive and innate immunity within a broader
535 immunological landscape of the fibrotic niche. Since our data indicate redundancy between
536 $CXCR6^+$ lymphocytes in MASH, we suggest that targeting the myeloid cells responsible for
537 CXCL16 production and HSC activation in combination with anti-steatotics will yield superior anti-
538 fibrotic activity. In conclusion, our study demonstrates that myeloid cells are master regulators of
539 fibrosis and fibrosis-associated adaptive immunity, redefining the immune-mediated fibrotic niche
540 in MASH.

541 **Figures and figure legends**

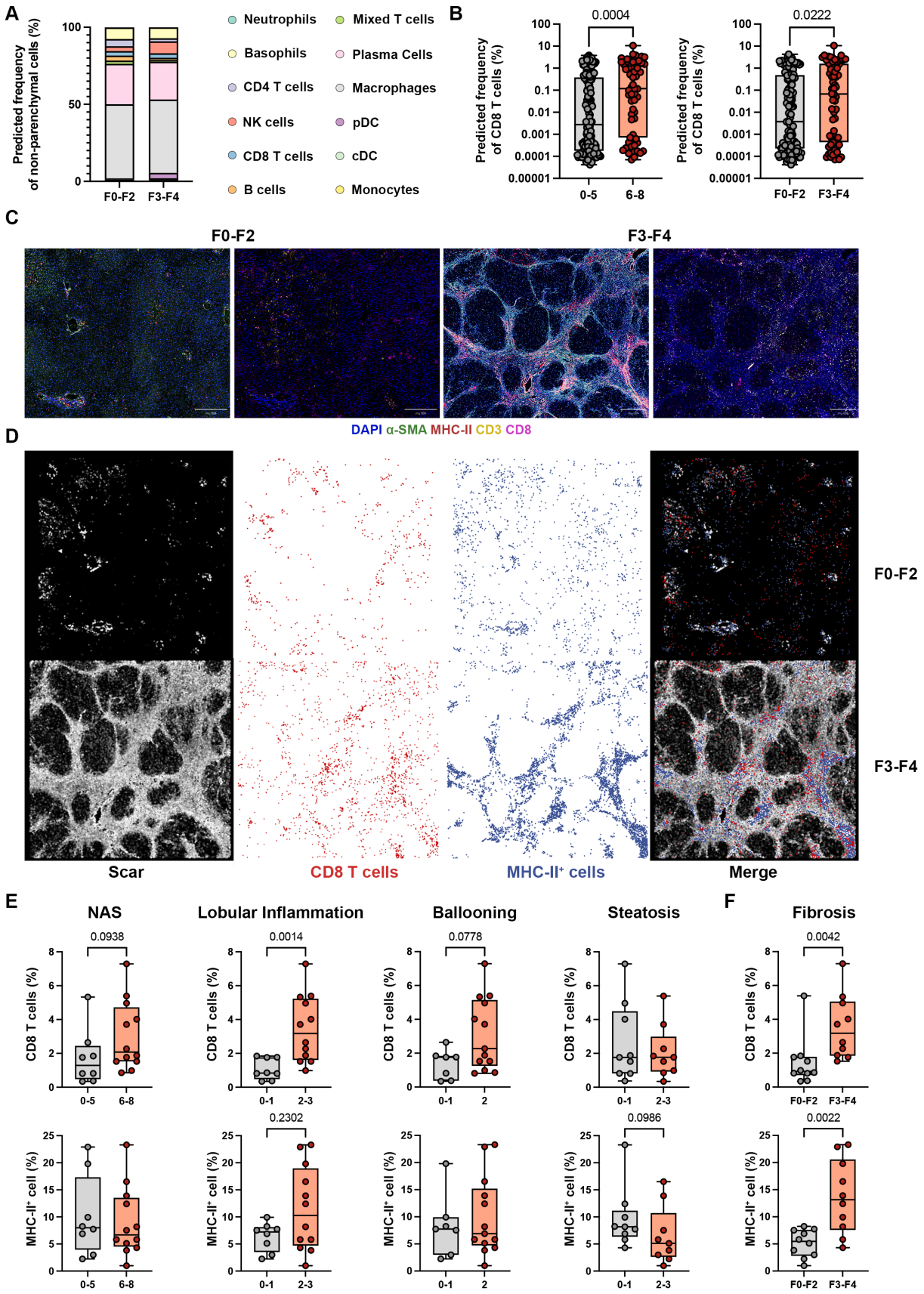
A
Predicted frequency of non-parenchymal cells (%)
100
50
0
F0-F2
F3-F4
Neutrophils
Mixed T cells
Basophils
Plasma Cells
CD4 T cells
Macrophages
NK cells
pDC
CD8 T cells
cDC
B cells
Monocytes
B
Predicted frequency of CD8 T cells (%)
0.0004
0.0222
0-5
6-8
F0-F2
F3-F4
C
F0-F2
F3-F4
DAPI α-SMA MHC-II CD3 CD8
D
F0-F2
F3-F4
Scar
CD8 T cells
MHC-II⁺ cells
Merge
E
NAS
Lobular Inflammation
Ballooning
Steatosis
F
Fibrosis
CD8 T cells (%)
MHC-II⁺ cell (%)
0.0938
0.0014
0.0778
0.0042
0.2302
0.0986
0.0022
0-5
6-8
0-1
2-3
2
F0-F2
F3-F4

542

543 **Figure 1: Accumulation of CD8 T cells and myeloid cells in scar in human MASH**

544 (A) Predicted frequency from deconvoluted bulk RNA-seq (GSE135251) of immune-cells within
545 the non-parenchymal fraction between F0-F2 and F3-F4 patients. (B) Box plot showing increased
546 predicted frequency of CD8 T cells in NAS 6-8 and F3-F4 patients. (C) Representative
547 immunofluorescence of α-SMA (green), MHC-II (red), CD3 (yellow) and CD8 (magenta) from F0-
548 F2 and F3-F4 patient liver sections. (D) cycIF representative images of liver sections showing
549 scar (α-SMA$^+$ cells, grey), CD3$^+$CD8$^+$ T cells (red), MHC-II$^+$ cells (blue) and merge overlay from
550 patients with minimal fibrosis (F0-F2) or severe fibrosis (F3-F4). (E-F) Box plots showing CD8$^+$ T
551 cells (top) and MHC-II$^+$ (bottom) cell frequencies from cycIF according to NAS, lobular
552 inflammation, ballooning, steatosis (E) and fibrosis (F) from 20 patients with MASH. Data are
553 presented as min – max values and median box plots. Box plot statistical analysis was performed
554 by Mann-Whitney test.

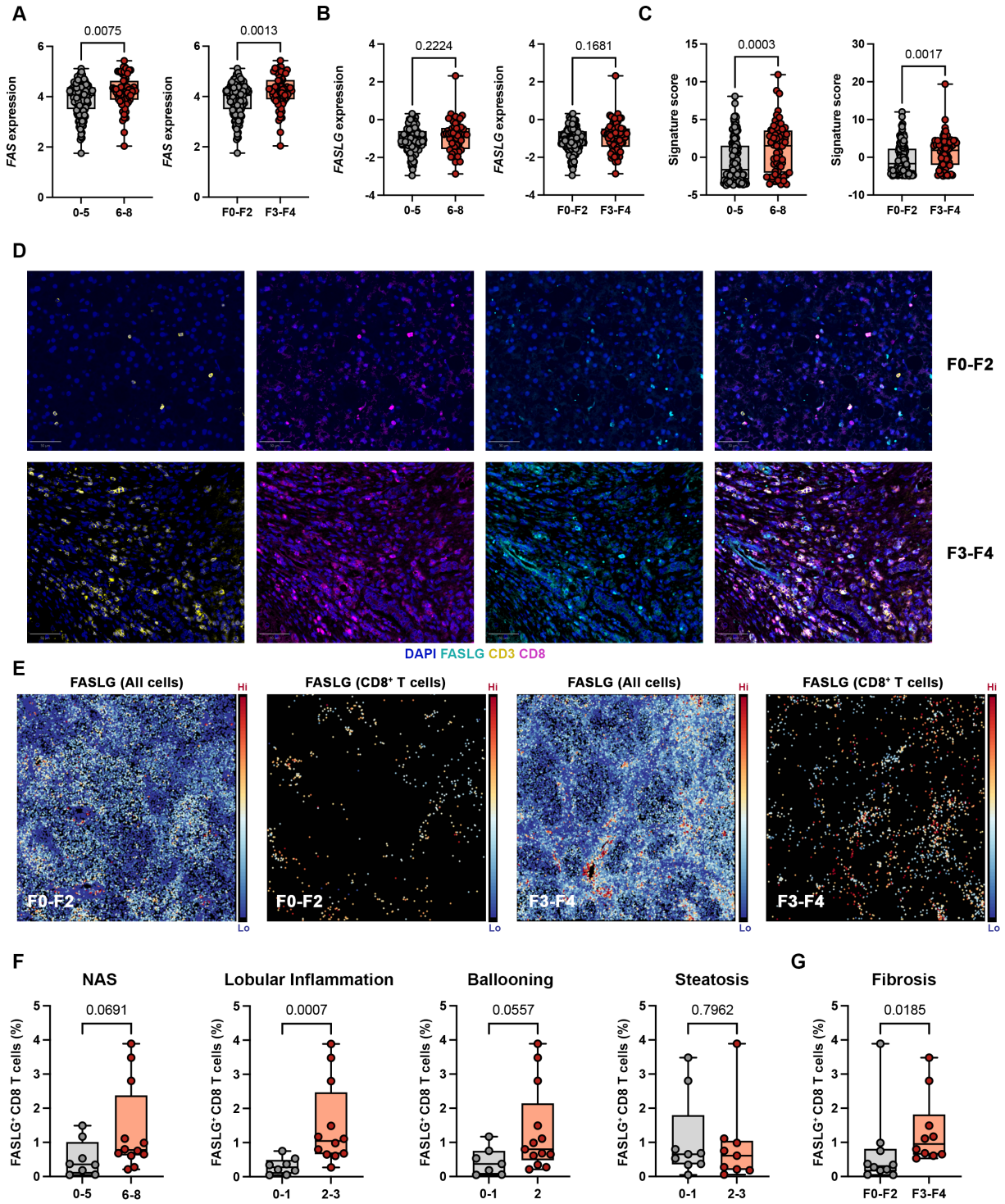
A
0.0075
FAS expression
0-5
6-8
0.0013
FAS expression
F0-F2
F3-F4
B
0.2224
FASLG expression
0-5
6-8
0.1681
FASLG expression
F0-F2
F3-F4
C
0.0003
Signature score
0-5
6-8
0.0017
Signature score
F0-F2
F3-F4
D
F0-F2
F3-F4
DAPI FASLG CD3 CD8
E
FASLG (All cells)
FASLG (CD8⁺ T cells)
FASLG (All cells)
FASLG (CD8⁺ T cells)
Hi
Lo
F0-F2
F0-F2
F3-F4
F3-F4
F
NAS
0.0691
Lobular Inflammation
0.0007
Ballooning
0.0557
Steatosis
0.7962
G
Fibrosis
0.0185
FASLG⁺ CD8 T cells (%)
0-5
6-8
0-1
2-3
0-1
2
0-1
2-3
F0-F2
F3-F4

555

556

557 **Figure 2: Accumulation of auto-aggressive FASLG$^+$ CD8 T cells in scar in human MASH**

558 (A-C) Bulk RNA-seq expression of *FAS* (A, global expression), *FASLG* (B, global expression) and
559 auto-aggressive signature score (C, in deconvoluted CD8 T cells) based on fibrosis score (F0-F2,
560 grey vs F3-F4, red). (D) Representative IF images of CD3 (yellow), CD8 (magenta) and FASLG
561 (cyan) from F0-F2 and F3-F4 MASH livers. (E) cycIF representative images showing expression
562 intensity (blue=low and red=high) of FASLG in all cells vs CD8 T cells from F0-F2 and F3-F4
563 MASH livers. (F-G) Box plots showing the frequency of FASLG$^+$ CD8 T cells with NAS, lobular
564 inflammation, ballooning, steatosis (F) and fibrosis (G). Data are presented as min – max values
565 and median box plots. Box plot statistical analysis was performed by Mann-Whitney test.

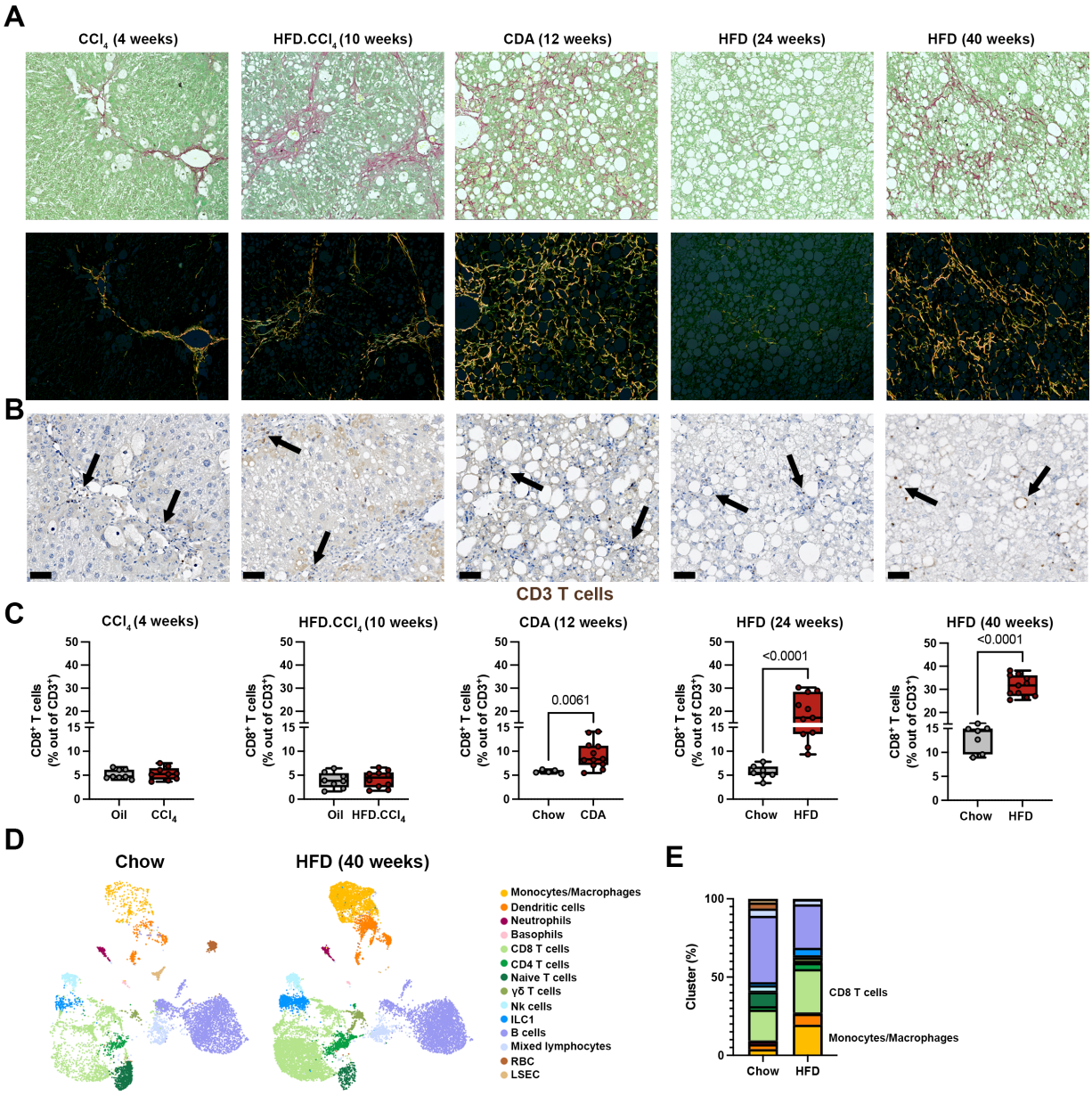
A
CCl4 (4 weeks)
HFD.CCl4 (10 weeks)
CDA (12 weeks)
HFD (24 weeks)
HFD (40 weeks)
B
CD3 T cells
C
CCl4 (4 weeks)
HFD.CCl4 (10 weeks)
CDA (12 weeks)
HFD (24 weeks)
HFD (40 weeks)
CD8+ T cells (% out of CD3+)
0.0061
<0.0001
<0.0001
Oil
CCl4
Oil
HFD.CCl4
Chow
CDA
Chow
HFD
Chow
HFD
D
Chow
HFD (40 weeks)
Monocytes/Macrophages
Dendritic cells
Neutrophils
Basophils
CD8 T cells
CD4 T cells
Naive T cells
γδ T cells
Nk cells
ILC1
B cells
Mixed lymphocytes
RBC
LSEC
E
Cluster (%)
CD8 T cells
Monocytes/Macrophages
Chow
HFD

566

567

568 **Figure 3. Chronic high-fat diet (HFD) leads to increased frequency of CD8 T cells in**
569 **preclinical MASH models.**
570 (A) Representative brightfield (top) and polarized light (bottom) picro Sirius Red images from 4
571 weeks of CCl_4, 10 weeks of HFD/CCl_4 ,12 weeks of CDA, or 24 and 40 weeks of HFD, respectively.
572 (B) Representative immunohistochemistry images of CD3 T cells in hepatic fibrotic regions of
573 mice challenged with CCl_4, HFD/CCl_4, CDA, 24 or 40 weeks HFD, respectively. (C) Box plots
574 showing the frequency of intrahepatic CD8 T cells from mice challenged with CCl_4, HFD/CCl_4,
575 CDA, 24- or 40 weeks HFD measured by flow cytometry, respectively. (D) UMAP visualization of
576 immune cells from scRNA-seq from chow (left) and HFD (right) livers at 40 weeks post study start
577 (n=3 mice per group). (E) Stacked bar chart showing the relative frequency of immune cells from
578 scRNA-seq. Data are presented as min – max values and median box plots. Box plot statistical
579 analysis was performed by Mann-Whitney test.

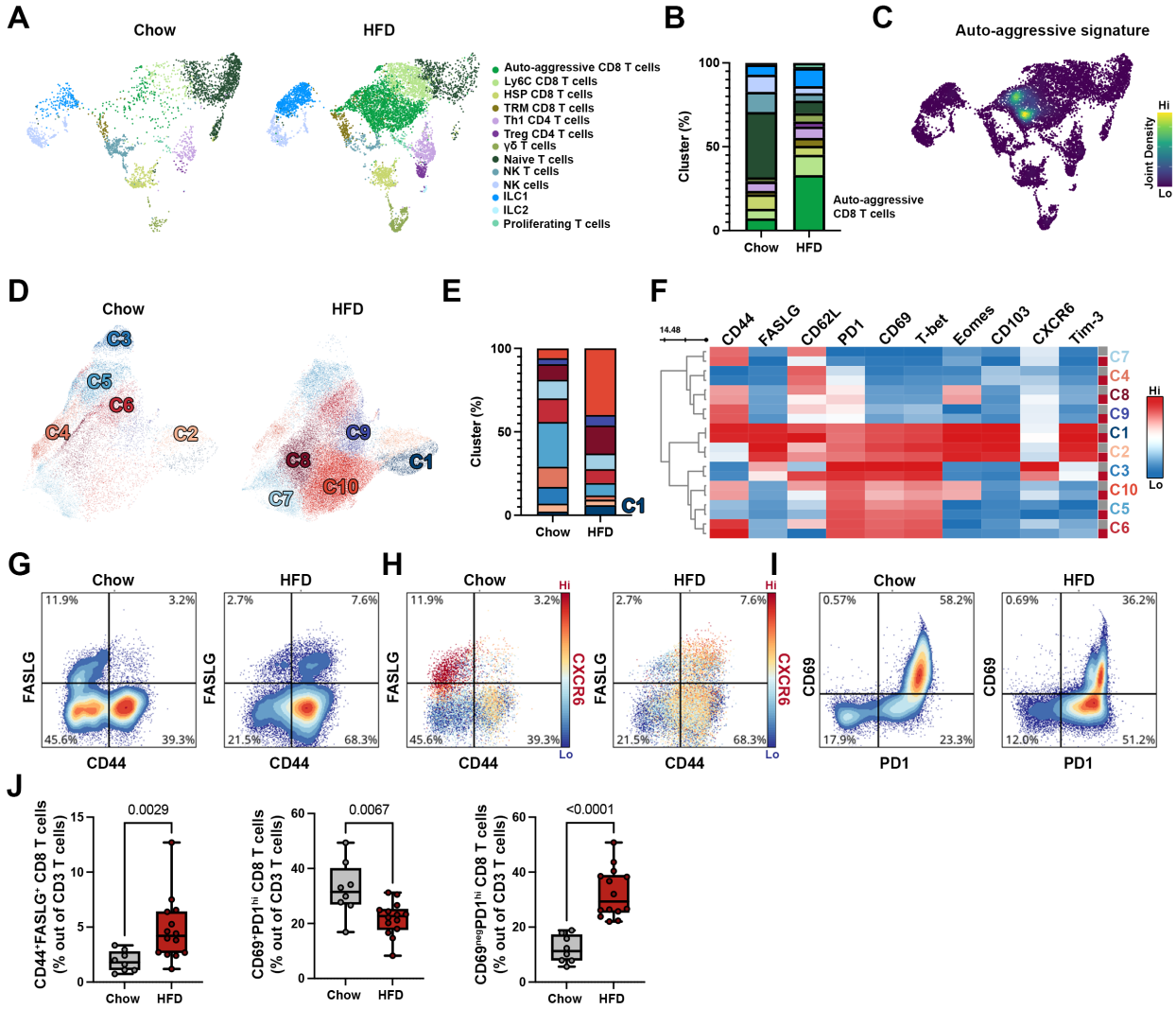
A
Chow
HFD
Auto-aggressive CD8 T cells
Ly6C CD8 T cells
HSP CD8 T cells
TRM CD8 T cells
Th1 CD4 T cells
Treg CD4 T cells
γδ T cells
Naive T cells
NK T cells
NK cells
ILC1
ILC2
Proliferating T cells
B
Cluster (%)
Auto-aggressive CD8 T cells
C
Auto-aggressive signature
Joint Density
Hi
Lo
D
C3
C5
C6
C4
C2
C9
C8
C1
C10
C7
E
Cluster (%)
C1
F
14.48
CD44
FASLG
CD62L
PD1
CD69
T-bet
Eomes
CD103
CXCR6
Tim-3
C7
C4
C8
C9
C1
C2
C3
C10
C5
C6
G
FASLG
CD44
11.9%
3.2%
45.6%
39.3%
2.7%
7.6%
21.5%
68.3%
H
CXCR6
11.9%
3.2%
45.6%
39.3%
2.7%
7.6%
21.5%
68.3%
I
CD69
PD1
0.57%
58.2%
17.9%
23.3%
0.69%
36.2%
12.0%
51.2%
J
CD44+FASLG+ CD8 T cells (% out of CD3 T cells)
0.0029
CD69+PD1hi CD8 T cells (% out of CD3 T cells)
0.0067
CD69negPD1hi CD8 T cells (% out of CD3 T cells)
<0.0001
Chow
HFD

580

581

582 **Figure 4. Accumulation of FASLG^{+} auto-aggressive CD8 T cells in chronic HFD-fed mice.**
583 (A) UMAP visualization of lymphocytes from chow (left) and HFD (right) livers after 40 weeks. (B)
584 Stacked bar chart showing the frequency of different lymphocyte subsets from panel A and the
585 accumulation of auto-aggressive CD8 T cells (green) in HFD livers. (C) Joint density
586 approximation of the auto-aggressive signature (*Cxcr6*, *Il2rb*, *Pdcd1*, *Fasl*, *Cd3e*) enabling the
587 identification of FASLG^{+} auto-aggressive CD8 T cells. (D) UMAP visualization of 10 CD8 T cell
588 clusters identified by flow cytometry. (E) Stacked bar chart showing relative frequency of the 10
589 CD8 T cell clusters, shown as C1 to C10 from bottom to top, between chow and HFD livers. (F)
590 Clustered heatmap showing the relative log2FC change in the MFI of markers on the 10 CD8 T
591 cell clusters (grey=chow and red=HFD). (G-H) Representative FACS plots showing increased
592 frequency of CD44^{+}FASLG^{+} CD8 T cells (G), overlayed with CXCR6 MFI (H). (I) Representative
593 FACS plots showing the decreased frequency of tissue resident memory-like CD8 T cells
594 (CD69^{+}PD1^{+}) in HFD livers. (J) Box plots showing the relative frequency of
595 CD44^{+}FASLG^{+}CXCR6^{+} (auto-aggressive) CD8 T cells (left), CD69^{+}PD1^{hi} CD8 T cells (middle) and
596 CD69^{neg}PD1^{hi} CD8 T cells (right). Data are presented as min – max values and median box plots.
597 Box plot statistical analysis was performed by Mann-Whitney test.

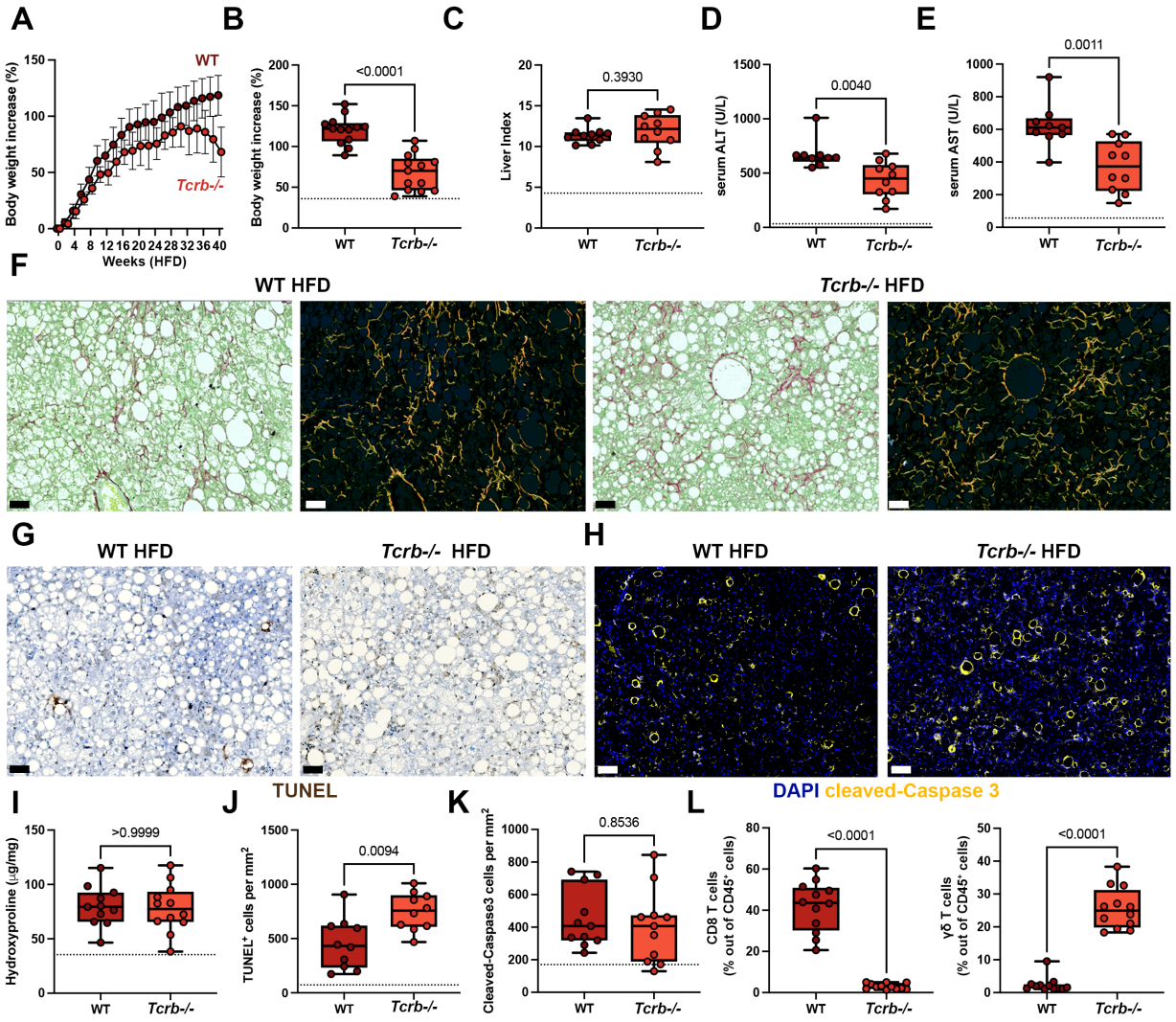
A
B
C
D
E
WT
Tcrb-/-
Body weight increase (%)
Weeks (HFD)
<0.0001
Body weight increase (%)
Liver Index
0.3930
serum ALT (U/L)
0.0040
serum AST (U/L)
0.0011
WT
Tcrb-/-
F
WT HFD
Tcrb-/- HFD
G
WT HFD
Tcrb-/- HFD
H
WT HFD
Tcrb-/- HFD
TUNEL
DAPI cleaved-Caspase 3
I
J
K
L
Hydroxyproline (µg/mg)
>0.9999
TUNEL+ cells per mm2
0.0094
Cleaved-Caspase3 cells per mm2
0.8536
CD8 T cells (% out of CD45+ cells)
<0.0001
γδ T cells (% out of CD45+ cells)
<0.0001

598

599 **Figure 5. *Tcrb* deficiency does not mitigates steatosis, epithelial/hepatocellular death or**
600 **fibrosis in chronic HFD-fed mice.**
601 (A-E) Body weight curves (A), percent increase in body weight after 40 weeks of HFD (B), liver
602 index (C), serum ALT (D) and serum AST (E) between WT (dark red) and *Tcrb-/-* (red) HFD-treated
603 mice. (F-H) Representative picro Sirius Red brightfield and polarized light (F), TUNEL staining (G)
604 and cleaved-Caspase 3 immunofluorescent (H) images from WT and *Tcrb-/-* HFD-treated mice.
605 (I-J) Box plots showing the quantification of hydroxyproline (I), $TUNEL^+$ cells per mm^2 (J) and
606 cleaved-Caspase 3^+ cells (K) between WT and *Tcrb-/-* HFD-treated mice. (L) Box plots showing
607 the relative frequency of conventional CD8 T cells and γδ T cells between WT and *Tcrb-/-* HFD-
608 treated mice. Data are presented as min – max values and median box plots. Box plot statistical
609 analysis was performed by Mann-Whitney test.

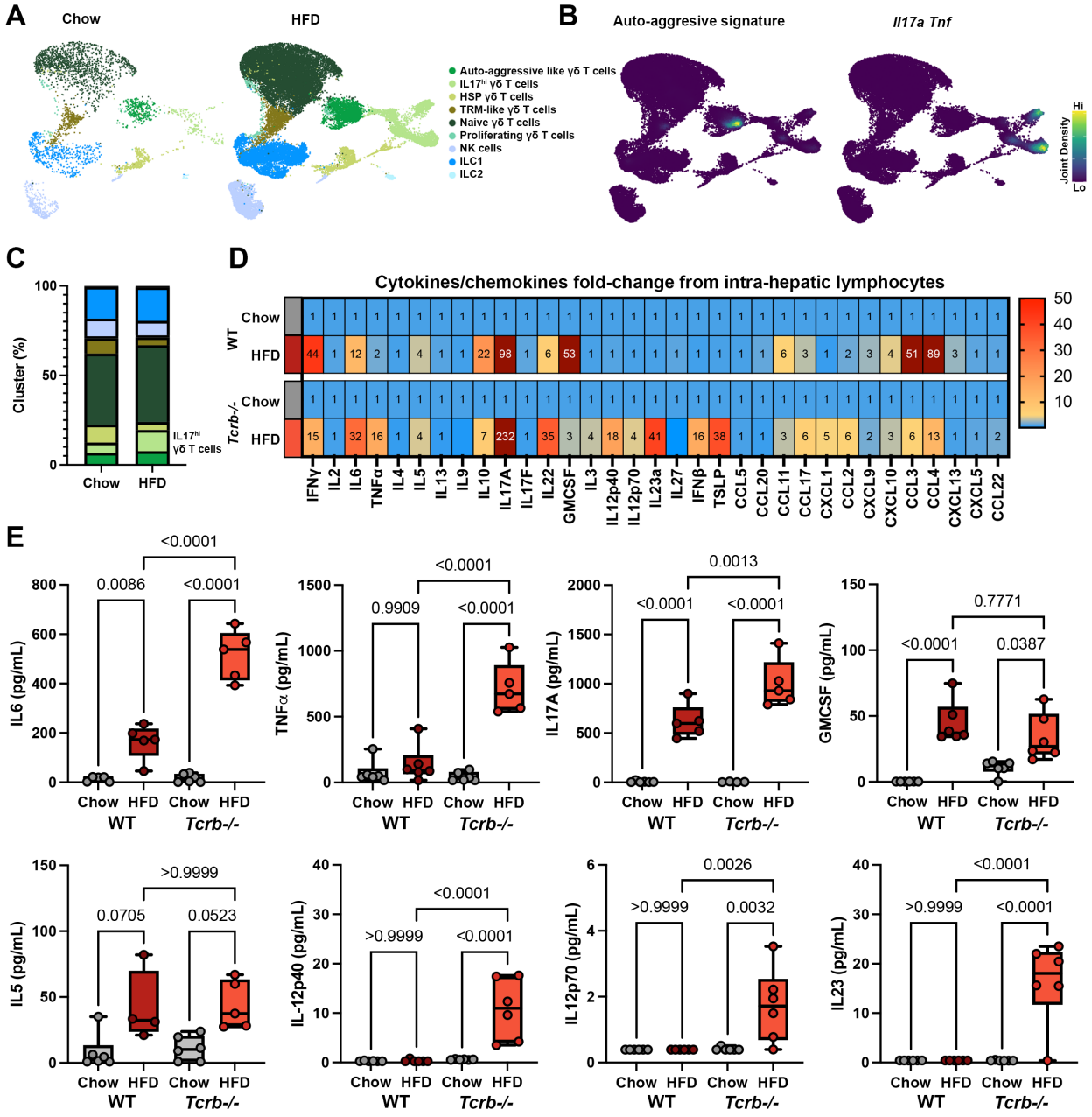
A
Chow
HFD
Auto-aggressive like γδ T cells
IL17hi γδ T cells
HSP γδ T cells
TRM-like γδ T cells
Naive γδ T cells
Proliferating γδ T cells
NK cells
ILC1
ILC2
B
Auto-aggresive signature
Il17a Tnf
Hi
Joint Density
Lo
C
Cluster (%)
IL17hi γδ T cells
Chow
HFD
D
Cytokines/chemokines fold-change from intra-hepatic lymphocytes
WT
Tcrb-/-
Chow
HFD
IFNγ IL2 IL6 TNFα IL4 IL5 IL13 IL9 IL10 IL17A IL17F IL22 GMCSF IL3 IL12p40 IL12p70 IL23a IL27 IFNβ TSLP CCL5 CCL20 CCL11 CCL17 CXCL1 CCL2 CXCL9 CXCL10 CCL3 CCL4 CXCL13 CXCL5 CCL22
E
IL6 (pg/mL)
TNFα (pg/mL)
IL17A (pg/mL)
GMCSF (pg/mL)
IL5 (pg/mL)
IL-12p40 (pg/mL)
IL12p70 (pg/mL)
IL23 (pg/mL)
Chow HFD Chow HFD
WT Tcrb-/-

610

611

612 **Figure 6. Loss of conventional CD8 T cells exacerbates pro-fibrotic type 3 inflammation**

613 (A) UMAP visualization of lymphocytes from livers of *Tcrb-/-* mice on chow or HFD at 40 weeks
614 by scRNA-seq. (B) Joint density expression of the auto-aggressive signature (*Cxcr6*, *Il2rb*, *Pdcd1*,
615 *Fasl*, *Cd3e*) (left), *Il17a* and *Tnf* (right). (C) Stacked bar chart showing the frequency of
616 lymphocytes from *Tcrb-/-* mice on chow or HFD for 40 weeks. (D) Heatmap of cytokines, fold
617 change to chow (grey) mice, from re-stimulated IHLs isolated from WT (dark red) and *Tcrb-/-* (red)
618 HFD mice after 40 weeks. (E) Box plots showing the intrahepatic levels of type 3 (IL-6, TNFα,
619 IL17A, GMCSF), type 2 (IL-5) and T-cell inducing cytokines (IL-12p40, IL-12p70, IL-23) between
620 chow-fed (grey) and chronic HFD-fed WT (dark red) and *Tcrb-/-* (red) mice. Data are presented
621 as min – max values and median box plots. Box plot statistical analysis was performed by ANOVA
622 and Tukey post-hoc test.

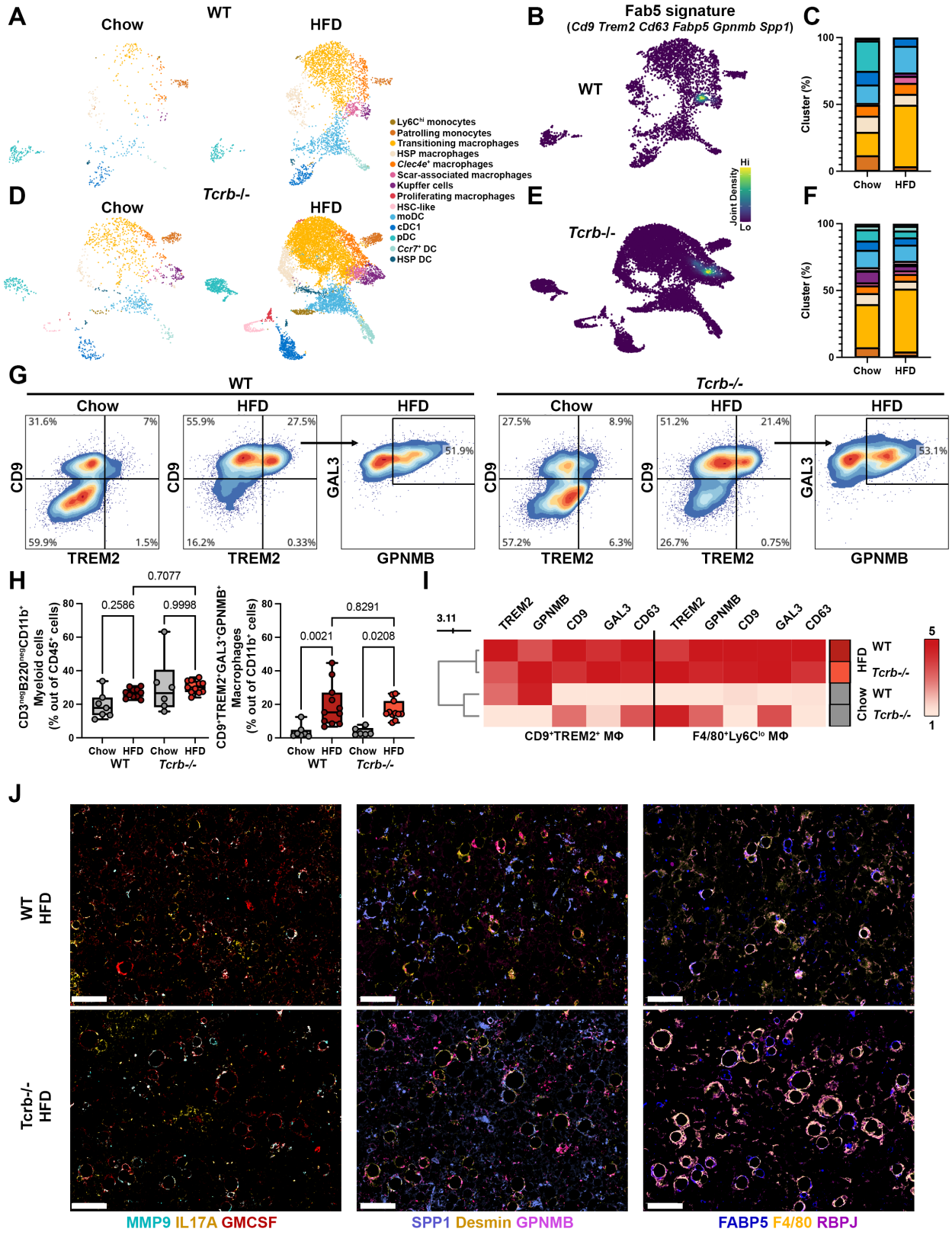
A
Chow
WT
HFD
Ly6C^hi monocytes
Patrolling monocytes
Transitioning macrophages
HSP macrophages
Clec4e+ macrophages
Scar-associated macrophages
Kupffer cells
Proliferating macrophages
HSC-like
moDC
cDC1
pDC
Ccr7+ DC
HSP DC
D
Chow
Tcrb-/-
HFD
B
Fab5 signature
(Cd9 Trem2 Cd63 Fabp5 Gpnmb Spp1)
WT
Tcrb-/-
Hi
Joint Density
Lo
E
C
Cluster (%)
100
50
0
Chow
HFD
F
G
WT
Tcrb-/-
Chow
HFD
HFD
CD9
TREM2
GAL3
GPNMB
31.6%
7%
59.9%
1.5%
55.9%
27.5%
16.2%
0.33%
51.9%
27.5%
8.9%
57.2%
6.3%
51.2%
21.4%
26.7%
0.75%
53.1%
H
CD3^neg B220^neg CD11b^+ Myeloid cells (% out of CD45^+ cells)
CD9^+ TREM2^+ GAL3^+ GPNMB^+ Macrophages (% out of CD11b^+ cells)
0.7077
0.2586
0.9998
0.8291
0.0021
0.0208
Chow
HFD
WT
Tcrb-/-
I
3.11
TREM2
GPNMB
CD9
GAL3
CD63
CD9^+TREM2^+ MΦ
F4/80^+Ly6C^lo MΦ
HFD
Chow
WT
Tcrb-/-
5
1
J
WT
HFD
Tcrb-/-
HFD
MMP9 IL17A GMCSF
SPP1 Desmin GPNMB
FABP5 F4/80 RBPJ

623

624 **Figure 7. SPP1^{+} scar-associated macrophages (SAMs) accumulate and persist in fibrosis,**
625 **independently of conventional CD8 T cells.**
626 (A,D) UMAP visualization of myeloid cells from livers of WT (A) and *Tcrb-/-* (D) mice after 40
627 weeks of chow (left) or HFD (right) by scRNA-seq. (B,E) Joint density expression of the pro-fibrotic
628 Fab5 signature (*Spp1, Gpnmb, Fabp5, Cd63, Cd9*) in WT (B) and *Tcrb-/-* (E) mice. (C,F) Stacked
629 bar chart showing the frequency of myeloid cell clusters between chow and HFD WT (C) and
630 *Tcrb-/-* (F) mice after 40 weeks. (G) Representative FACS plots showing the identification of
631 SPP1^{+} SAMs by flow cytometry using co-expression of CD9, TREM2, Galectin-3 and GPNMB in
632 F4/80^{+}Ly6C^{lo} macrophages from WT (left) and *Tcrb-/-* (right) mice. (H) Box plots showing the
633 relative frequency of myeloid cells from CD45^{+} cells (left) and the relative frequency of
634 CD9^{+}TREM2^{+}Galectin-3^{+}GPNMB^{+} SAMs from CD11b^{+} cells (right) between WT and *Tcrb-/-* mice
635 after 40 weeks on either chow or HFD. (I) Clustered heatmap showing the log2FC (scaled from 1
636 to 5) expression of scar-associated markers on F4/80^{+}Ly6C^{lo} or F4/80^{+}Ly6C^{lo}CD9^{+}TREM2^{lo}
637 macrophages between WT and *Tcrb-/-* mice at 40 weeks on either chow or chronic HFD. (J)
638 Representative immunofluorescent images from WT and *Tcrb-/-* mice after 40 weeks of HFD: left
639 panel for MMP9 (cyan), IL17A (yellow) and GMCSF (red), middle panel for SPP1 (light blue),
640 Desmin (yellow) and GPNMB (pink) and right panel for FABP5 (blue), F4/80 (yellow) and RBPJ
641 (magenta). Data are presented as min – max values and median box plots. Box plot statistical
642 analysis was performed by ANOVA and Tukey post-hoc test.
643

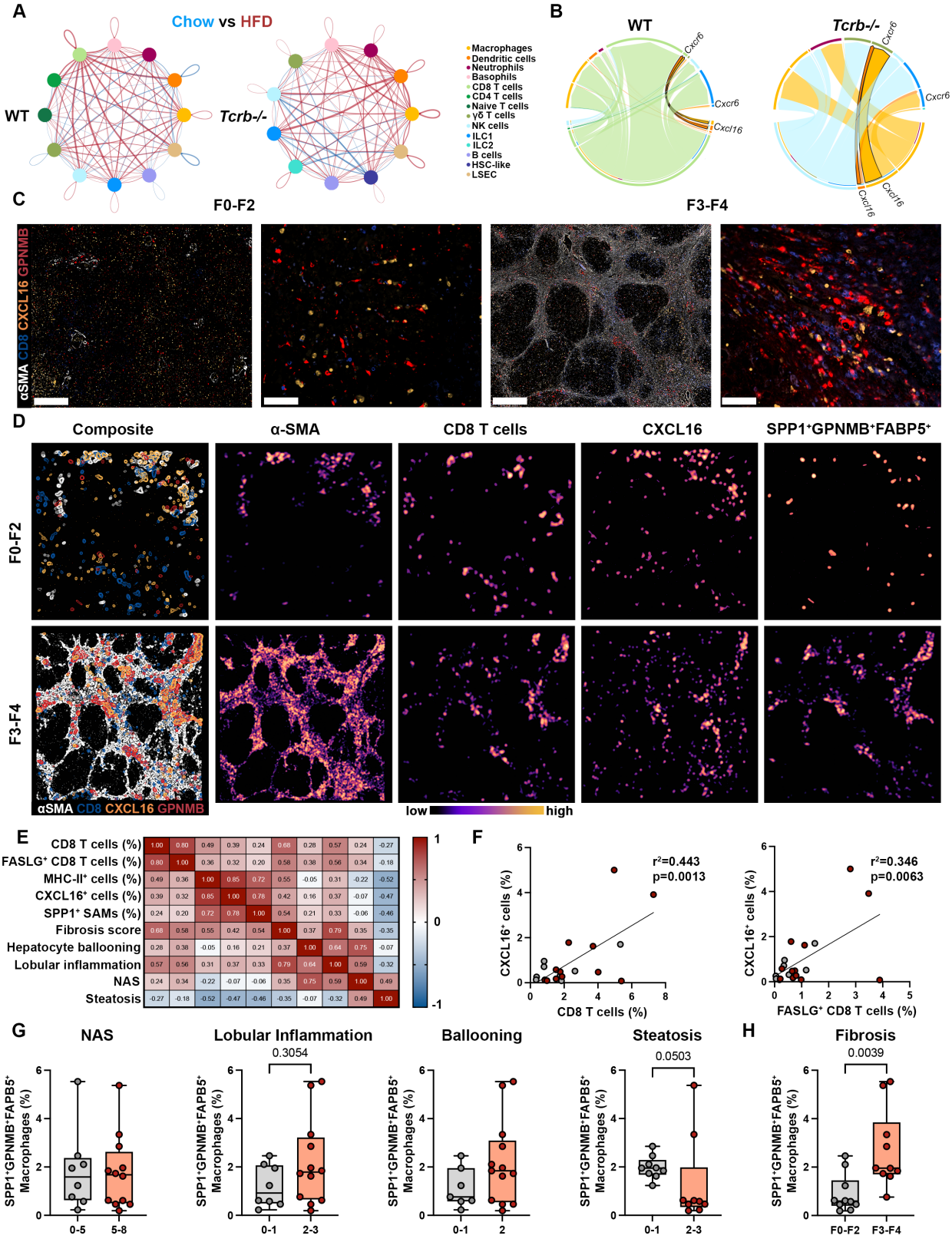
A
Chow vs HFD
WT
Tcrb-/-
Macrophages
Dendritic cells
Neutrophils
Basophils
CD8 T cells
CD4 T cells
Naive T cells
γδ T cells
NK cells
ILC1
ILC2
B cells
HSC-like
LSEC
B
WT
Tcrb-/-
Cxcr6
Cxcl16
C
F0-F2
F3-F4
αSMA CD8 CXCL16 GPNMB
D
Composite
α-SMA
CD8 T cells
CXCL16
SPP1⁺GPNMB⁺FABP5⁺
F0-F2
F3-F4
αSMA CD8 CXCL16 GPNMB
low
high
E
CD8 T cells (%)
FASLG⁺ CD8 T cells (%)
MHC-II⁺ cells (%)
CXCL16⁺ cells (%)
SPP1⁺ SAMs (%)
Fibrosis score
Hepatocyte ballooning
Lobular inflammation
NAS
Steatosis
F
r²=0.443
p=0.0013
CXCL16⁺ cells (%)
CD8 T cells (%)
r²=0.346
p=0.0063
FASLG⁺ CD8 T cells (%)
G
NAS
Lobular Inflammation
Ballooning
Steatosis
0.3054
0.0503
SPP1⁺GPNMB⁺FAPB5⁺ Macrophages (%)
0-5
5-8
0-1
2-3
2
H
Fibrosis
0.0039
F0-F2
F3-F4

644

645

646 **Figure 8. Myeloid cells expression of CXCL16 recruits CXCR6$^+$ T cells to the scar.**
647 (A) Circle plot showing the differential number of interactions between chow (blue) and HFD (red)
648 in WT (left) and *Tcrb-/-* (right) mice after 40 weeks by scRNA-seq. (B) Chord diagram visualizing
649 upregulated ligands mapped to their receptors in WT (left) and *Tcrb-/-* (right) mice. Black outline
650 highlights interactions between myeloid *Cxcl16* and conventional as well as γδ T cell *Cxcr6*
651 relative expression by scRNA-seq. (C) Representative immunofluorescent images of α-SMA
652 (white), CD8 (blue), CXCL16 (orange) and GPNMB (red) from F0-F2 (left) and F3-F4 (right) MASH
653 livers. (D) cycIF representative images showing the overlaid composite density of α-SMA (white),
654 CD8 (blue), CXCL16 (orange) and GPNMB (red) and the relative density of cells positive for α-
655 SMA, CD8, CXCL16, and GPNMB. (E) Heatmap showing spearman correlation (-1 to 1) between
656 the frequencies of CD8 T cells, FASLG$^+$ CD8 T cells, CXCL16$^+$ cells, MHC-II$^+$ cells, SPP1$^+$ SAMs,
657 fibrosis, hepatocyte ballooning, lobular inflammation, NAS and steatosis. (F) Spearman
658 correlation between the frequency of CXCL16$^+$ cells and the frequency of CD8 T cells (left) or
659 FASLG$^+$ CD8 T cells (right) in MASH livers. (G-H) Box plots showing the frequency of
660 SPP1$^+$GPNMB$^+$FABP5$^+$ SAMs with NAS, lobular inflammation, ballooning, steatosis (G) and
661 fibrosis (H). Data are presented as min – max values and median box plots. Box plot statistical
662 analysis was performed by Mann-Whitney test.

Figure S1

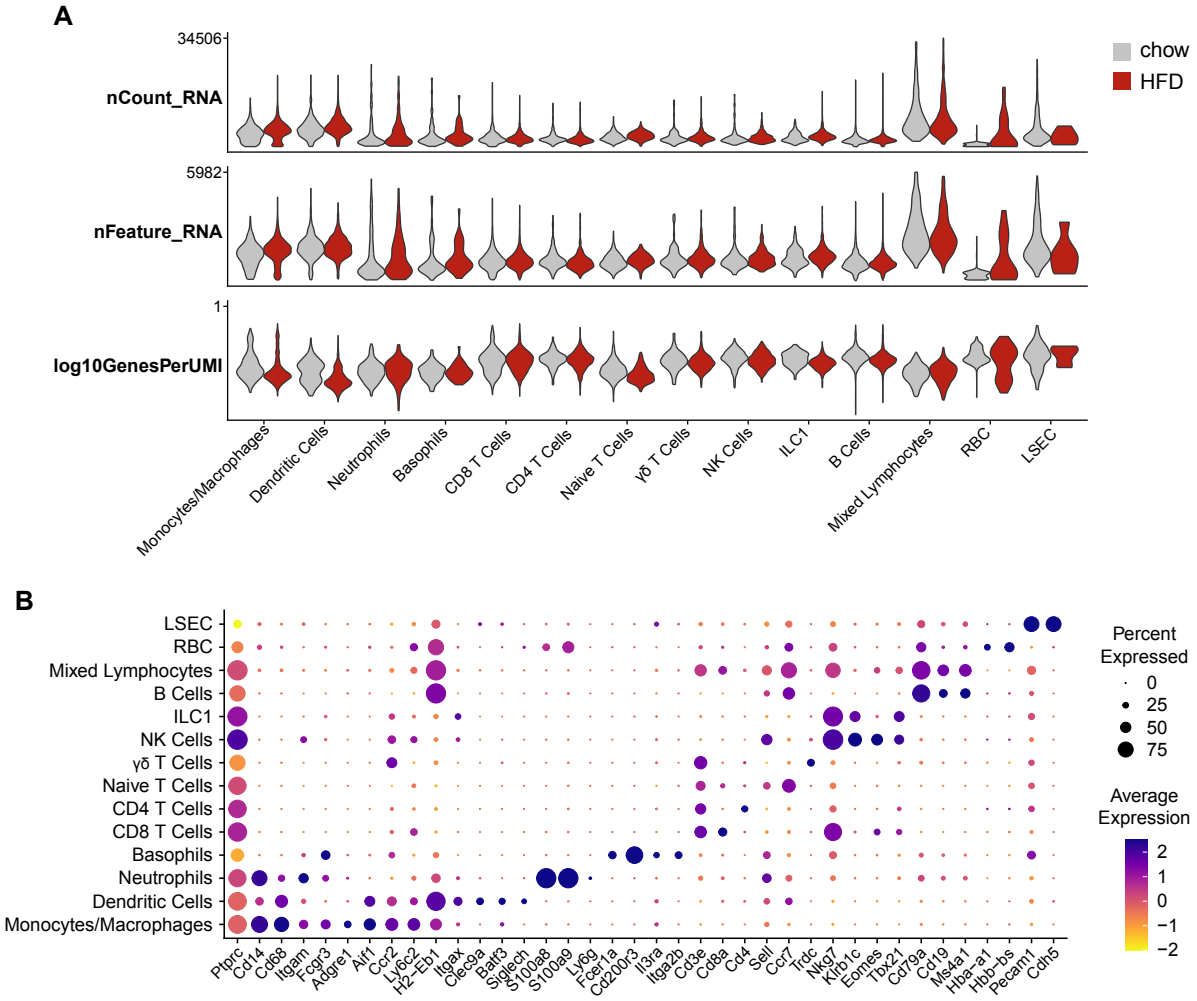

Supplementary Figure 1. Livers of chow- and HFD-fed wild-type (WT) mice profiled by scRNA-seq.

(A) Stacked violin plots of UMI, gene expression, and cell complexity by cell type in chow (grey) and HFD-fed (red) WT mice after 40 weeks of diet. (B) Dot plot of global marker gene expression in chow and HFD-fed WT mice combined.

Figure S2

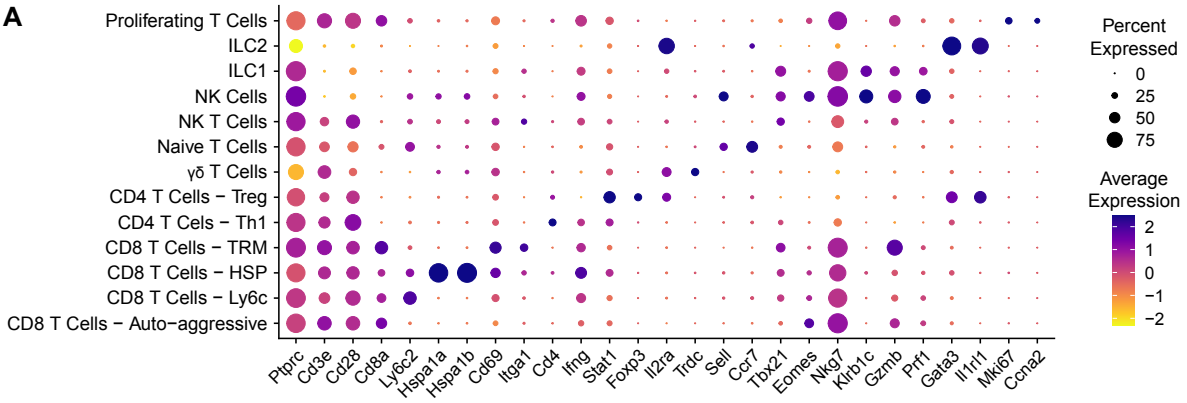

Supplementary Figure 2. WT liver lymphocyte gene expression by scRNA-seq.

(A) Dot plot of marker gene expression in subclustered lymphocytes from livers of chow and HFD-fed WT mice combined.

Figure S3

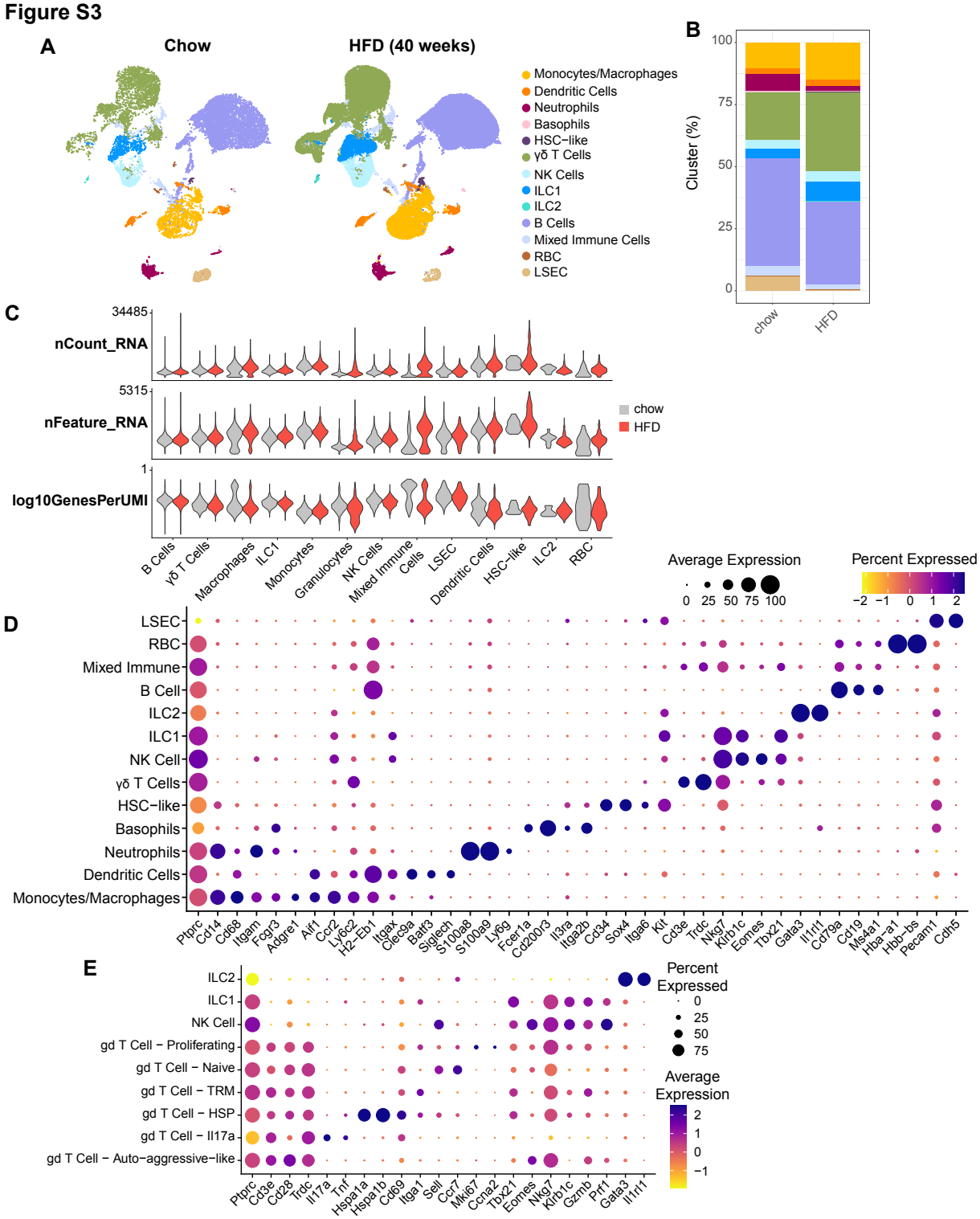

673

674

675

676 **Supplementary Figure 3. Livers of chow- and HFD-fed *Tcrb*$^{-/-}$ mice profiled by scRNA-seq.**
677 (A) Split UMAP of scRNA-seq global cell annotations from chow and HFD-fed *Tcrb*-/- mice after
678 40 weeks of diet. (B) Relative abundancies of global populations detected by scRNA-seq. (C)
679 Stacked violin plots of UMI, gene expression, and cell complexity by cell type in chow (grey) and
680 HFD-fed (red) *Tcrb*-/- mice. (D-E) Dot plots of global (D) and lymphocyte (E) marker gene
681 expression in livers of chow- and HFD-fed *Tcrb*-/- mice combined.

Figure S4

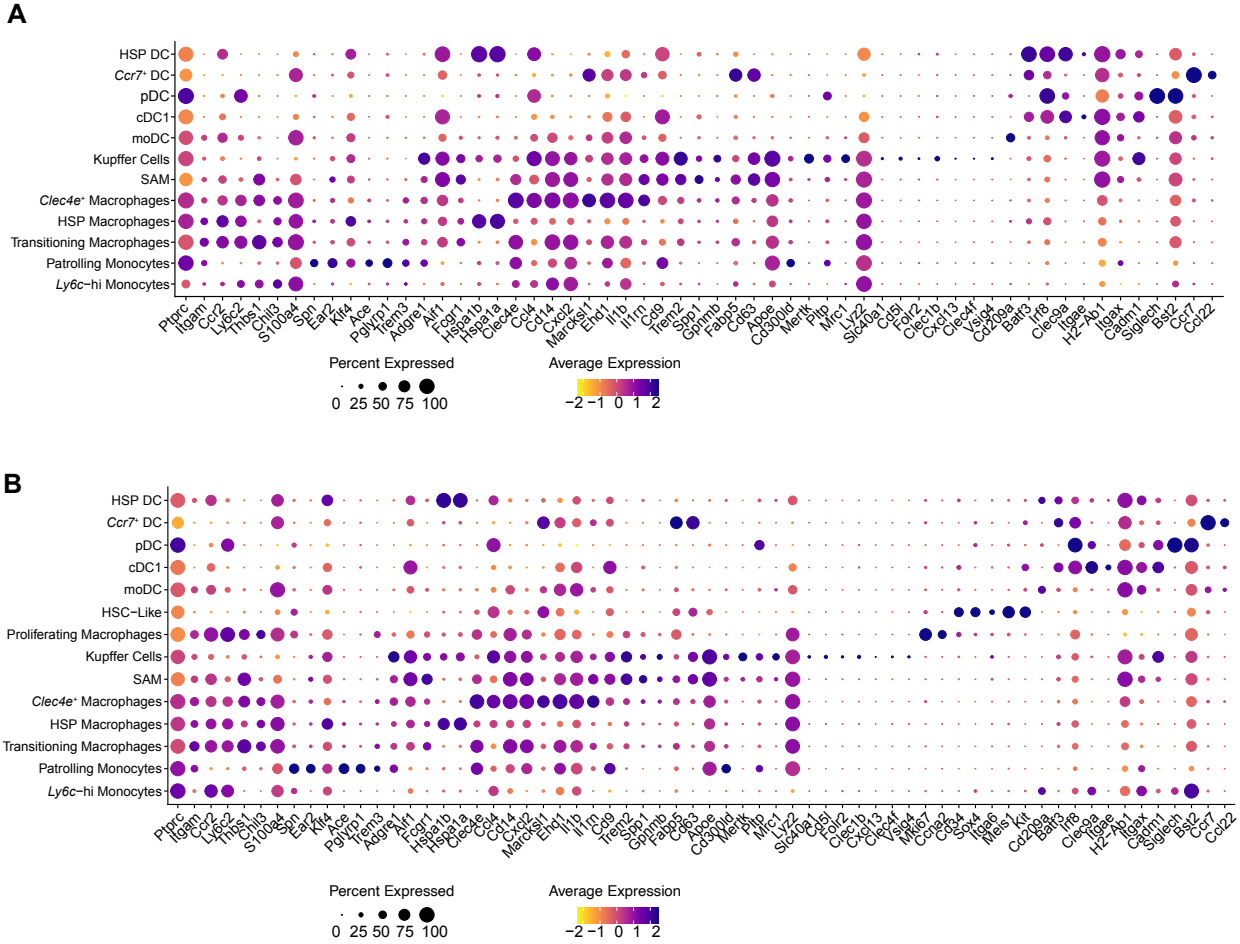

682

683 **Supplementary Figure 4. MASH liver myeloid gene expression by scRNA-seq.**

684 Dot plots of marker gene expression in combined chow- and HFD-fed WT mice (A) and *Tcrb*-/-

685 mice (B).

Figure S5

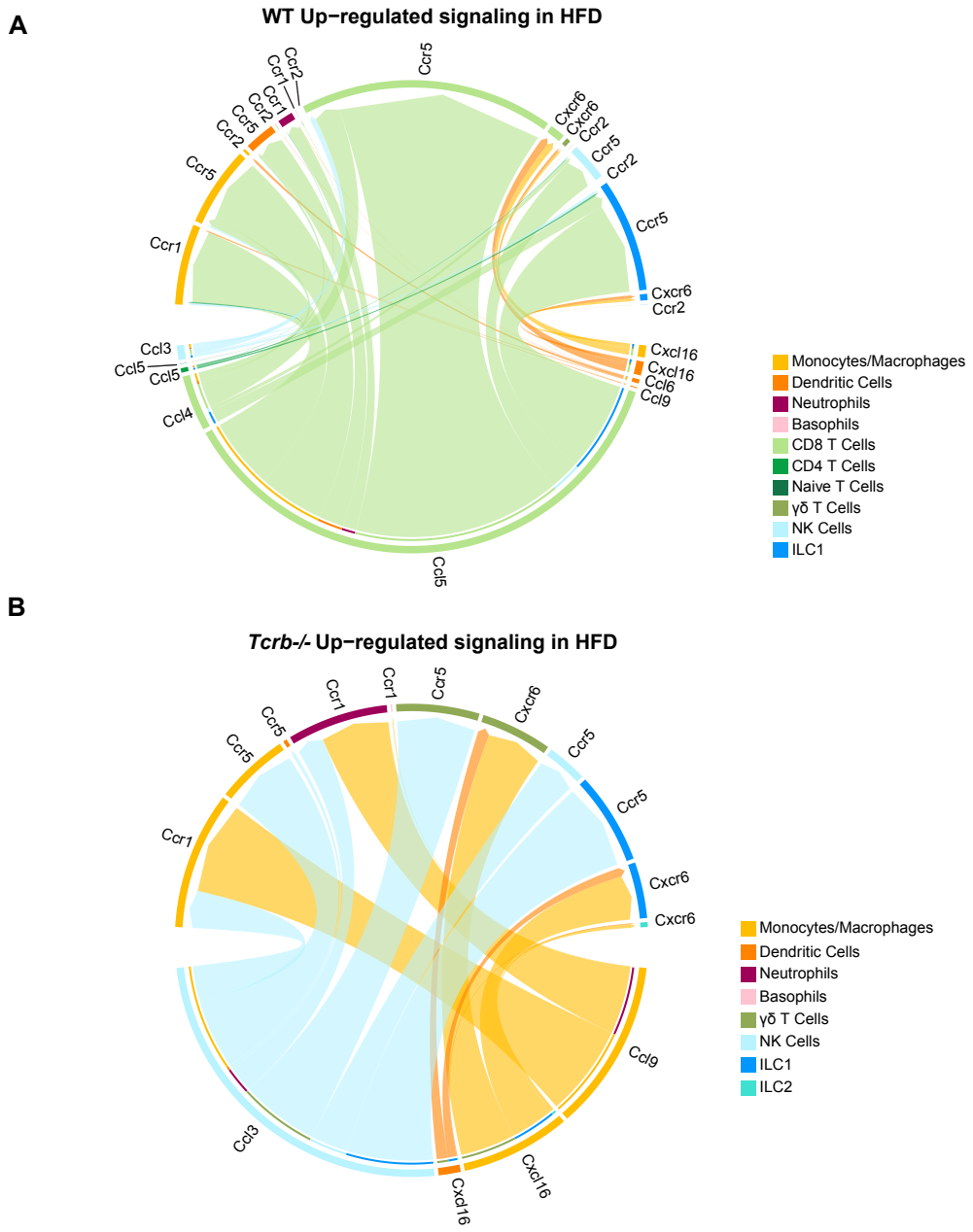

686

687 **Supplementary Figure 5. MASH liver chemokine/receptor interaction predictions from**

688 **scRNA-seq.**

689 Interactions upregulated in livers of HFD-fed WT (A) and *Tcrb-/-* (B) compared to chow-fed mice.

690 **Table S1. Patient metadata**

Patient ID	Disease	Fibrosis Stage	Hepatocyte Ballooning	Lobular Inflammation	NAS	Steatosis
F202288354388482	MASLD/MASH	4	1	1	3	1
F269667491781714	MASLD/MASH	1	2	2	7	3
F25230374217327	MASLD/MASH	3	0	3	3	0
F60076066942084	MASLD/MASH	4	2	3	6	1
F93815000985241	MASLD/MASH	4	2	3	6	1
F164630764073724	MASLD/MASH	0	0	1	3	2
F18870497925578	MASLD/MASH	3	1	2	3	0
F54808383304812	MASLD/MASH	2	2	2	7	3
F89655557507529	MASLD/MASH	4	2	3	5	0
F160333745451172	MASLD/MASH	0	0	1	3	2
F194072749341725	MASLD/MASH	4	2	3	8	3
F228919843573023	MASLD/MASH	4	2	3	5	0
F17160862857391	MASLD/MASH	4	2	3	5	0
F51999294867643	MASLD/MASH	3	2	3	7	2
F89045601851397	MASLD/MASH	2	2	3	7	2
F224751406165187	MASLD/MASH	0	2	1	3	0
F12855615291317	MASLD/MASH	1	1	1	5	3
F47702485095320	MASLD/MASH	1	1	1	3	1
F82540773355965	MASLD/MASH	0	1	1	5	3
F118489267437699	MASLD/MASH	1	1	1	4	2

691

692 **Table S2. Flow cytometry antibodies**

Target	Fluorophore	Clone	Panel
Trem2	FITC	78.18	SAMs
CD45	A700	30-F11	SAMs
GPNMB	e660	CTSREVL	SAMs
CD9	APC-Fire750	MZ3	SAMs
CD3	BUV395	145-2C11	SAMs
B220	BUV395	RA3-6B2	SAMs
Siglec-F	BUV395	E50-2440	SAMs
NK1.1	BUV395	PK-136	SAMs
CD11b	BUV787	M1/70	SAMs
CD81	BV421	EAT2	SAMs
F4/80	BV605	T45-2342	SAMs
Galectin-3	PE	M3/38	SAMs
Ly6G	PE-CF594	1A8	SAMs
Ly6C	PECy7	HK1.4	SAMs
CD63	PerCP.Cy5.5	NVG2	SAMs
Galectin-3	PE	M3/38	SAMs
Ly6G	PE-CF594	1A8	SAMs
Ly6C	PE-Cy7	HK1.4	SAMs
F4/80	BB515	T45-2342	Lineage
CD11c	PerCP.Cy5.5	N418	Lineage
TCRgd	BV421	GL3	Lineage
CD11b	BV605	M1/70	Lineage
B220	BV786	RA3-6B2	Lineage
CD3	BUV395	145-2C11	Lineage
CD4	BUV496	GK1.5	Lineage
CD8	BUV787	53-6.7	Lineage
CD68	APC	FA-11	Lineage
CD45	A700	30-F11	Lineage
NK1.1	APC-Cy7	PK-136	Lineage
Siglec-F	PE	E50-2440	Lineage
Ly6G	PE-CF584	1A8	Lineage
Ly6C	PE-Cy7	HK1.4	Lineage
CD44	A488	KM81	CD8 T cell
CD45	A700	30-F11	CD8 T cell
FASL	APC	MFL3	CD8 T cell
CD62L	APC-Cy7	MEL-14	CD8 T cell
CD3	BUV395	145-2C11	CD8 T cell

CD4	BUV496	GK1.5	CD8 T cell
CD8	BUV787	53-6.7	CD8 T cell
PD1	BV421	J43	CD8 T cell
CD69	BV605	H1-2F3	CD8 T cell
Tbet	BV785	O4-46	CD8 T cell
Eomes	PE	X4-83	CD8 T cell
CD103	PE-CF594	M290	CD8 T cell
CXCR6	PE-Cy7	SA051D1	CD8 T cell
Tim-3	PerCP-CY5.5	RMT3-23	CD8 T cell

693

694 **Table S3. Human cycIF antibodies**

Antibody	Catalog #	Company	Isotype	Clone
CD3e	MA5-16622	ThermoFisher Scientific	Rat	cd3-12
CD8a	NBP2-32836	Novus Biologicals	Mouse	C8/114B
Tim-3	AF2365	R&D	Goat	pAb
PD-1	367402	Biolegend	Mouse	NAT105
CXCL16	AF976	R&D Systems	Goat	pAb
FasLG	BS-0216R	Bioss	Rabbit	pAb
IL-17	AF-317-NA	R&D Systems	Goat	pAb
FABP5	MAB3077	R&D Systems	Rat	311215
PD-1	367402	Biolegend	Mouse	NAT105
Smooth muscle actin (SMA)	MAB1420	R&D Systems	Mouse	1A4
GPNMB/Osteoactivin	AF2550	R&D Systems	Goat	pAb
CD63	ab134045	Abcam	Rabbit	EPR5702
Galectin 3	NBP2-16589	Novus	Rabbit	pAb
Spp1/Osteopontin	AF1433	R&D Systems	Goat	pAb
PD-L1	AF156	R&D Systems	Goat	pAb
HLA-DR	NBP2-53380	Novus Biologicals	Mouse	CR3/43
CD248	379102	Biolegend	Mouse	B1/35
Desmin	PA5-16705	ThermoFisher Scientific	Rabbit	pAb
Podoplanin	AF3670	R&D Systems	Sheep	pAb

695

696 **Table S4. Mouse cycIF antibodies**

Antibody	Catalog #	Company	Isotype	Clone
S100A8/9	NBP2-27067	Novus	Rat	63N13G5
FABP5	AF1476	R&D Systems	Goat	pAb
IL-17A	PAA063Mu01	Cloud-Clone Corp	Rabbit	pAb
GMCSF	PAA045Mu01	Cloud-Clone Corp	RAbbit	pAb
MMP9	AF909	R&D Systems	Goat	pAb
IBA1	PA5-143572	ThermoFisher Scientific	Chicken	pAb
SPP1	AF808	R&D Systems	Goat	pAb
GPNMB	NBP1-69389	R&D Systems	Rabbit	pAb
Desmin	PA5-85187	ThermoFisher Scientific	Rabbit	pAb
Galectin-3	AF1197	R&D Systems	Goat	pAb
Clec4f	AF2784	R&D Systems	Goat	pAb
F4/80	70076	Cell Signaling Technology	Rabbit	D2S9R
RBPJ	5313	Cell Signaling Technology	Rabbit	D10A4
CD206	AF2335	R&D Systems	Goat	pAb

697

698 **Abbreviations**

699 CCl_4, carbon tetrachloride

700 CDA, choline-deficient diet

701 CDHFD, choline-deficient high-fat diet

702 CPM, counts per million

703 cycIF, cyclic immunofluorescence

704 DC, dendritic cell

705 DMN, dimethylnitrosamine

706 ECM, extracellular matrix

707 FACS, fluorescence-activated cell sorting

708 FBS, fetal bovine serum

709 FFPE, formalin-fixed paraffin-embedded

710 HBV and HCV, hepatitis B virus and hepatitis C virus, respectively

711 HFD, high-fat diet

712 HSC, hepatic stellate cell

713 IF, immunofluorescence

714 IHL, intrahepatic leukocyte

715 MASLD, metabolic dysfunction-associated steatotic liver disease

716 MASH, metabolic dysfunction-associated steatohepatitis

717 MCDD, methionine and choline-deficient diet

718 MDM, monocyte-derived macrophage

719 NAFLD, non-alcoholic fatty liver disease (*now referred to as MASLD*)

720 NAS, NAFLD activity score

721 NASH, non-alcoholic steatohepatitis (*now referred to as MASH*)

722 PBS, phosphate buffered saline

723 SAM, scar-associated macrophage

724 scRNA-seq, single cell RNA-seq

725 TRM, tissue-resident macrophage

726 WT, wild-type

727

728 **Financial support**

729 This study was financed by Pfizer Inc.

730

731 **Conflict of interest**

732 C.L, K.L.D., S.M.C., S.A., M.H.W., K.B., S.D., T.A.W., K.M.H., T.F. are or J.M., F.S., C.W., X.C.,

733 A.M.S.B. were employees of Pfizer Inc.

734

735 **Author contributions**

736 Acquisition, analysis and interpretation of data: C.L, K.L.D., S.M.C., S.A., M.H.W., K.B, S.D., J.M.,

737 F.S., C.W., X.C., A.M.S.B., K.M.H., T.F. Drafting and writing of the manuscript: C.L., K.L.D, T.F.

738 Critical revision of the manuscript for important intellectual content: T.A.W. Study concept, design

739 supervision: A.M.S.B., T.A.W., K.M.H., T.F.

740

741 **Data availability**

742 The datasets generated and/or analyzed during the present study are available from the

743 corresponding author upon reasonable, scientifically justified request.

744

745 **Acknowledgements**

746 We thank the Pfizer Flow Cytometry, Optical Microscopy, High Content Imaging, and Next-

747 Generation Sequencing Technology Centers. K.L.D. thanks the Pfizer Postdoctoral Fellowship

748 Program for support.

References

1 Le, P. *et al.* Estimated Burden of Metabolic Dysfunction-Associated Steatotic Liver Disease in US Adults, 2020 to 2050. *JAMA Netw Open* **8**, e2454707, doi:10.1001/jamanetworkopen.2024.54707 (2025).

2 Xiang, L. *et al.* Safety and efficacy of GLP-1/FGF21 dual agonist HEC88473 in MASLD and T2DM: A randomized, double-blind, placebo-controlled study. *J Hepatol* **82**, 967-978, doi:10.1016/j.jhep.2024.12.006 (2025).

3 Sanyal, A. J. *et al.* Phase 3 Trial of Semaglutide in Metabolic Dysfunction-Associated Steatohepatitis. *N Engl J Med* **392**, 2089-2099, doi:10.1056/NEJMoa2413258 (2025).

4 Hammerich, L. & Tacke, F. Hepatic inflammatory responses in liver fibrosis. *Nat Rev Gastroenterol Hepatol* **20**, 633-646, doi:10.1038/s41575-023-00807-x (2023).

5 Foster, R. G., Golden-Mason, L., Rutebemberwa, A. & Rosen, H. R. Interleukin (IL)-17/IL-22-producing T cells enriched within the liver of patients with chronic hepatitis C viral (HCV) infection. *Dig Dis Sci* **57**, 381-389, doi:10.1007/s10620-011-1997-z (2012).

6 Li, J. *et al.* Significance of the balance between regulatory T (Treg) and T helper 17 (Th17) cells during hepatitis B virus related liver fibrosis. *PLoS One* **7**, e39307, doi:10.1371/journal.pone.0039307 (2012).

7 Zhao, L. *et al.* Interleukin-17 contributes to the pathogenesis of autoimmune hepatitis through inducing hepatic interleukin-6 expression. *PLoS One* **6**, e18909, doi:10.1371/journal.pone.0018909 (2011).

8 Claassen, M. A., de Knegt, R. J., Tilanus, H. W., Janssen, H. L. & Boonstra, A. Abundant numbers of regulatory T cells localize to the liver of chronic hepatitis C infected patients and limit the extent of fibrosis. *J Hepatol* **52**, 315-321, doi:10.1016/j.jhep.2009.12.013 (2010).

9 Wasmuth, H. E. *et al.* Antifibrotic effects of CXCL9 and its receptor CXCR3 in livers of mice and humans. *Gastroenterology* **137**, 309-319, 319 e301-303, doi:10.1053/j.gastro.2009.03.053 (2009).

10 Teixeira, R., Marcos, L. A. & Friedman, S. L. Immunopathogenesis of hepatitis C virus infection and hepatic fibrosis: New insights into antifibrotic therapy in chronic hepatitis C. *Hepatol Res* **37**, 579-595, doi:10.1111/j.1872-034X.2007.00085.x (2007).

11 Fabre, T. *et al.* Type 3 cytokines IL-17A and IL-22 drive TGF-beta-dependent liver fibrosis. *Sci Immunol* **3**, doi:10.1126/sciimmunol.aar7754 (2018).

12 Rong, G. *et al.* Imbalance between T helper type 17 and T regulatory cells in patients with primary biliary cirrhosis: the serum cytokine profile and peripheral cell population. *Clin Exp Immunol* **156**, 217-225, doi:10.1111/j.1365-2249.2009.03898.x (2009).

13 Ichiki, Y. *et al.* T cell immunity in autoimmune hepatitis. *Autoimmun Rev* **4**, 315-321, doi:10.1016/j.autrev.2005.01.005 (2005).

14 Russell, J. Q. *et al.* Liver damage preferentially results from CD8(+) T cells triggered by high affinity peptide antigens. *J Exp Med* **188**, 1147-1157, doi:10.1084/jem.188.6.1147 (1998).

15 Shi, Z., Wakil, A. E. & Rockey, D. C. Strain-specific differences in mouse hepatic wound healing are mediated by divergent T helper cytokine responses. *Proc Natl Acad Sci U S A* **94**, 10663-10668, doi:10.1073/pnas.94.20.10663 (1997).

16 Hyon, M. K., Kwon, E., Choi, H. J. & Kang, B. C. Dimethylnitrosamine-induced liver fibrosis and recovery in NOD/SCID mice. *J Vet Med Sci* **73**, 739-745, doi:10.1292/jvms.10-0311 (2011).

17 Hernandez-Gea, V. & Friedman, S. L. Pathogenesis of liver fibrosis. *Annu Rev Pathol* **6**, 425-456, doi:10.1146/annurev-pathol-011110-130246 (2011).

18 Hart KM, F. T., Sciurba JS, Gieseck RL III, Borthwick LA, Vannella KM, Acciani TH, de Queiroz Prado R, Thompson RW, White S, Soucy G, Bilodeau M, Ramalingam TR,

Shoukry NH, and Wynn TA. Type-2 immunity is protective in metabolic disease but exacerbates NAFLD collaboratively with TGF-β. *Sci Transl Med* **In press** (2017).

19 Wolf, M. J. *et al.* Metabolic activation of intrahepatic CD8+ T cells and NKT cells causes nonalcoholic steatohepatitis and liver cancer via cross-talk with hepatocytes. *Cancer Cell* **26**, 549-564, doi:10.1016/j.ccell.2014.09.003 (2014).

20 Deczkowska, A. *et al.* XCR1(+) type 1 conventional dendritic cells drive liver pathology in non-alcoholic steatohepatitis. *Nat Med* **27**, 1043-1054, doi:10.1038/s41591-021-01344-3 (2021).

21 Dudek, M. *et al.* Auto-aggressive CXCR6(+) CD8 T cells cause liver immune pathology in NASH. *Nature* **592**, 444-449, doi:10.1038/s41586-021-03233-8 (2021).

22 Flores Molina, M. *et al.* Visualization, Quantification, and Mapping of Immune Cell Populations in the Tumor Microenvironment. *J Vis Exp*, doi:10.3791/60740 (2020).

23 Fabre, T. *et al.* Identification of a broadly fibrogenic macrophage subset induced by type 3 inflammation. *Sci Immunol* **8**, eadd8945, doi:10.1126/sciimmunol.add8945 (2023).

24 Schindelin, J. *et al.* Fiji: an open-source platform for biological-image analysis. *Nat Methods* **9**, 676-682, doi:10.1038/nmeth.2019 (2012).

25 Botvinik-Nezer, R. *et al.* Variability in the analysis of a single neuroimaging dataset by many teams. *Nature* **582**, 84-88, doi:10.1038/s41586-020-2314-9 (2020).

26 McGinnis, C. S. *et al.* MULTI-seq: sample multiplexing for single-cell RNA sequencing using lipid-tagged indices. *Nat Methods* **16**, 619-626, doi:10.1038/s41592-019-0433-8 (2019).

27 Hao, Y. *et al.* Dictionary learning for integrative, multimodal and scalable single-cell analysis. *Nat Biotechnol* **42**, 293-304, doi:10.1038/s41587-023-01767-y (2024).

28 Young, M. D. & Behjati, S. SoupX removes ambient RNA contamination from droplet-based single-cell RNA sequencing data. *Gigascience* **9**, doi:10.1093/gigascience/giaa151 (2020).

29 Stoeckius, M. *et al.* Cell Hashing with barcoded antibodies enables multiplexing and doublet detection for single cell genomics. *Genome Biol* **19**, 224, doi:10.1186/s13059-018-1603-1 (2018).

30 Hafemeister, C. & Satija, R. Normalization and variance stabilization of single-cell RNA-seq data using regularized negative binomial regression. *Genome Biol* **20**, 296, doi:10.1186/s13059-019-1874-1 (2019).

31 Alquicira-Hernandez, J. & Powell, J. E. Nebulosa recovers single-cell gene expression signals by kernel density estimation. *Bioinformatics* **37**, 2485-2487, doi:10.1093/bioinformatics/btab003 (2021).

32 Butler, A., Hoffman, P., Smibert, P., Papalexi, E. & Satija, R. Integrating single-cell transcriptomic data across different conditions, technologies, and species. *Nat Biotechnol* **36**, 411-420, doi:10.1038/nbt.4096 (2018).

33 Chu, T., Wang, Z., Pe'er, D. & Danko, C. G. Cell type and gene expression deconvolution with BayesPrism enables Bayesian integrative analysis across bulk and single-cell RNA sequencing in oncology. *Nat Cancer* **3**, 505-517, doi:10.1038/s43018-022-00356-3 (2022).

34 Love, M. I., Huber, W. & Anders, S. Moderated estimation of fold change and dispersion for RNA-seq data with DESeq2. *Genome Biol* **15**, 550, doi:10.1186/s13059-014-0550-8 (2014).

35 Carenzo, A. *et al.* hacksig: a unified and tidy R framework to easily compute gene expression signature scores. *Bioinformatics* **38**, 2940-2942, doi:10.1093/bioinformatics/btac161 (2022).

36 Satija, R., Farrell, J. A., Gennert, D., Schier, A. F. & Regev, A. Spatial reconstruction of single-cell gene expression data. *Nat Biotechnol* **33**, 495-502, doi:10.1038/nbt.3192 (2015).

37 Govaere, O. *et al.* Transcriptomic profiling across the nonalcoholic fatty liver disease spectrum reveals gene signatures for steatohepatitis and fibrosis. *Sci Transl Med* **12**, doi:10.1126/scitranslmed.aba4448 (2020).
38 Vacca, M. *et al.* An unbiased ranking of murine dietary models based on their proximity to human metabolic dysfunction-associated steatotic liver disease (MASLD). *Nat Metab* **6**, 1178-1196, doi:10.1038/s42255-024-01043-6 (2024).
39 Guo, W. *et al.* Notch signaling regulates macrophage-mediated inflammation in metabolic dysfunction-associated steatotic liver disease. *Immunity* **57**, 2310-2327 e2316, doi:10.1016/j.immuni.2024.08.016 (2024).
40 Burtis, A. E. C. *et al.* Ag-driven CD8 + T cell clonal expansion is a prominent feature of MASH in humans and mice. *Hepatology* **81**, 591-608, doi:10.1097/HEP.0000000000000971 (2025).
41 Dywicki, J. *et al.* From model to man: Understanding Tregs' dual role in MASLD. *JHEP Reports* **7**, doi:10.1016/j.jhepr.2025.101619 (2025).
42 Hammerich, L. & Tacke, F. Role of gamma-delta T cells in liver inflammation and fibrosis. *World J Gastrointest Pathophysiol* **5**, 107-113, doi:10.4291/wjgp.v5.i2.107 (2014).
43 Ma, H. Y. *et al.* IL-17 signaling in steatotic hepatocytes and macrophages promotes hepatocellular carcinoma in alcohol-related liver disease. *J Hepatol* **72**, 946-959, doi:10.1016/j.jhep.2019.12.016 (2020).
44 Kim, J. Y. *et al.* ER Stress Drives Lipogenesis and Steatohepatitis via Caspase-2 Activation of S1P. *Cell* **175**, 133-145 e115, doi:10.1016/j.cell.2018.08.020 (2018).
45 Fabre, T., Kared, H., Friedman, S. L. & Shoukry, N. H. IL-17A Enhances the Expression of Profibrotic Genes through Upregulation of the TGF-beta Receptor on Hepatic Stellate Cells in a JNK-Dependent Manner. *J Immunol* **193**, 3925-3933, doi:10.4049/jimmunol.1400861 (2014).
46 Wehr, A. *et al.* Pharmacological inhibition of the chemokine CXCL16 diminishes liver macrophage infiltration and steatohepatitis in chronic hepatic injury. *PLoS One* **9**, e112327, doi:10.1371/journal.pone.0112327 (2014).
47 Krenkel, O. *et al.* Therapeutic inhibition of inflammatory monocyte recruitment reduces steatohepatitis and liver fibrosis. *Hepatology* **67**, 1270-1283, doi:10.1002/hep.29544 (2018).
48 Lefebvre, E. *et al.* Antifibrotic Effects of the Dual CCR2/CCR5 Antagonist Cenicriviroc in Animal Models of Liver and Kidney Fibrosis. *PLoS One* **11**, e0158156, doi:10.1371/journal.pone.0158156 (2016).
49 Baeck, C. *et al.* Pharmacological inhibition of the chemokine CCL2 (MCP-1) diminishes liver macrophage infiltration and steatohepatitis in chronic hepatic injury. *Gut* **61**, 416-426, doi:10.1136/gutjnl-2011-300304 (2012).
50 Anstee, Q. M. *et al.* Tropifexor plus cenicriviroc combination versus monotherapy in nonalcoholic steatohepatitis: Results from the phase 2b TANDEM study. *Hepatology* **78**, 1223-1239, doi:10.1097/HEP.0000000000000439 (2023).